


RESEARCH ARTICLE

Artificial instabilities of finite elements for nonlinear elasticity: Analysis and remedies

Simon Bieber¹  | Ferdinando Auricchio² | Alessandro Reali² | Manfred Bischoff¹

¹Institute for Structural Mechanics, University of Stuttgart, Stuttgart, Germany

²Department of Civil Engineering and Architecture, University of Pavia, Pavia, Italy

Correspondence

Manfred Bischoff, Institute for Structural Mechanics, University of Stuttgart, Pfaffenwaldring 7, 70550 Stuttgart, Germany.

Email: Bischoff@ibb.uni-stuttgart.de

Funding information

Deutsche Forschungsgemeinschaft (DFG), Grant/Award Number: BI 722/11-1; Italian Ministry of University and Research (MIUR), Grant/Award Number: 20173C478N

Summary

Within the framework of plane strain nonlinear elasticity, we present a discussion on the stability properties of various Enhanced Assumed Strain (EAS) finite element formulations with respect to physical and artificial (hourglassing) instabilities. By means of a linearized buckling analysis we analyze the influence of element formulations on the geometric stiffness and provide new mechanical insights into the hourglassing phenomenon. Based on these findings, a simple strategy to avoid hourglassing for compression problems is proposed. It is based on a modification of the discrete Green-Lagrange strain, simple to implement and generally applicable. The stabilization concept is tested for various popular element formulations (namely EAS elements and the assumed stress element by Pian and Sumihara). A further aspect of the present contribution is a discussion on proper benchmarking of finite elements in the context of hourglassing. We propose a simple bifurcation problem for which analytical solutions are readily available in the literature. It is tailored for an in-depth stability analysis of finite elements and allows a reliable assessment of its stability properties.

KEYWORDS

artificial instability, enhanced assumed strain, finite elasticity, hourglassing

1 | INTRODUCTION

The incentive for the present work emanates from the unsolved problem of artificial instabilities encountered in large strain nonlinear finite element analysis in the field of solid and structural mechanics. The problem that is addressed is briefly summarized in the following.

Standard Galerkin finite elements may suffer from locking and perform too stiff in certain situations. One of the first ideas to remove locking was to use reduced integration but it was soon detected that this may lead to artificial instabilities.^{1,2} Such artificial instabilities are often denoted as *hourglassing*, because in the pattern of the artificial buckling modes, pairs of elements resemble the shape of an hourglass. Later, hourglass stabilization has been developed to alleviate this problem, see for example, References 3,4. In the meantime, numerous alternative “unlocking” schemes have been developed, which are mostly stable in the linear case. For the important class of mixed finite elements in the linear regime, numerical stability can be guaranteed by the celebrated inf-sup-condition.⁵

In the context of nonlinear problems, however, the flexibility introduced by unlocking schemes may give rise to unphysical unstable configurations, even if full integration is used and the elements are stable in the linear case. This was first described by Wriggers and Reese⁶ and De Souza Neto et al.⁷ The problem appears to be intrinsic to many

This is an open access article under the terms of the [Creative Commons Attribution](https://creativecommons.org/licenses/by/4.0/) License, which permits use, distribution and reproduction in any medium, provided the original work is properly cited.

© 2023 The Authors. *International Journal for Numerical Methods in Engineering* published by John Wiley & Sons Ltd.

typical approaches that are taken to remove locking and is not an exclusive quality of only a few particular strategies in finite element technology. To the authors' best knowledge, in contrast to the linear case, there is no mathematical theory for numerical stability for general nonlinear problems. One of the reasons is that the exact solution may contain physical instabilities, such that naively requiring the finite element model to be stable, over all ranges of deformation, is not appropriate. Accordingly, finite element models should be able to capture physical instabilities, without presenting extra unphysical instabilities associated to numerical pathologies. The delicate distinction of pathological numerical instabilities and physical instabilities is one of the key challenges tackled in this paper.

Similar to physical instabilities, artificial, unphysical instabilities can be induced by geometric or material nonlinearity, see Reese et al.^{8,9} When trying to analyze the underlying effects, it is crucial to separate these two classes of nonlinear problems. In the following, we will therefore refer to *geometric hourglassing* for the former and *material hourglassing* for the latter case.

Despite the considerable amount of literature, the development of nonlinear finite elements has not reached the same level of maturity as it is the case in the linear regime. The following literature review is restricted to some selected works and we refer to the recent overview by Pfefferkorn and Betsch¹⁰ as well as Chap. 10 of Wriggers¹¹ for further references.

In analogy to geometric (structural) instabilities we introduce the term *geometric hourglassing* and relate it to artificial instabilities that occur under compressive stress states, triggered by negative geometric stiffness. First investigations by Simo and Armero¹² and Wriggers and Reese⁶ showed that this type of hourglassing occurs for Enhanced Assumed Strain elements (EAS)¹³ in the presence of large compressive strain and may be identified by negative eigenvalues of the element stiffness matrix. For rectangular elements it can be shown that the strain enhancement that eliminates shear locking is responsible for this pathology.

From an engineering viewpoint, this type of instability can be associated with “buckling on element level”, where the negative *geometric stiffness* triggers geometric hourglassing, see for example, Reese et al.⁸ and Wall et al.¹⁴ In Reference 14 it is shown that the well-known hourglass patterns can be explained by the violation of inter-element continuity, along with the equivalence of EAS elements and the method of incompatible modes. As the denomination “geometric hourglassing” suggests, this type of instabilities is strongly influenced by the element's *geometric* properties. Thus, for elements with a large aspect ratio, geometric hourglassing can already occur in small strain regimes, as descriptively shown in Sussmann and Bathe,¹⁵ see also the aspect ratio dependent modal analysis in Armero.¹⁶ Geometric hourglassing is not only restricted to EAS elements, but is also observed for other element formulations such as assumed stress elements¹⁷ and reduced integrated elements.¹⁸ As shown for the compression problem in Auricchio et al.¹⁹ (Sec. 6.1.2), some displacement-pressure type formulations may also suffer from geometric hourglassing, although less pronounced compared to standard EAS elements.

Many remedies against geometric hourglassing are, explicitly or implicitly, based on a modification of the geometric tangent. For the classical EAS formulation,¹² Korelc and Wriggers²⁰ proposed a simple modification of the enhanced shear strain, such that the geometric stiffness parts that trigger hourglassing are eliminated (cf. Section 2 in this work). The element shows no geometric hourglassing, but further technical modifications are required to ensure objectivity, see for example, References 10,21. With the same outcome, Wall et al.¹⁴ constructed a variational, deformation dependent stabilization procedure that eliminates the critical parts of the geometric stiffness for a special two-dimensional case. A similar philosophy was pursued by Reese et al.⁸ in the context of reduced integrated elements, combined with physical stabilization. They proposed to neglect the (destabilizing) geometric part of the hourglass “stabilization”. Other elements that are free from geometric hourglassing are the Cosserat point element by Nadler et al.²² and the EAS formulation by Mueller-Hoeppe et al.,²³ both incorporating linear elasticity theory for the construction of the higher order stiffness. However, in the present study we propose a more generally applicable concept with improved performance for nonlinear bending dominated problems.

Since the remedy of shear locking is critical with respect to geometric hourglassing, an obvious way to alleviate it is to simply accept shear locking and rely on formulations that exclusively deal with volumetric locking, for example, displacement-pressure type formulations²⁴ or reduced EAS or mixed formulations.^{17,25}

Apart from EAS related literature, other recent contributions to element technology for large strain problems are available. The authors want to highlight in particular the triangular element formulations with edge degrees of freedom of Neunteufel et al.,²⁶ the nonconforming formulations of Bayat et al.²⁷ as well as formulations based on a polyconvex structure of the strain energy functions.^{28,29} Each of the formulations show a good performance for the considered set of large strain compression problems. However, these discretization concepts are out of scope herein.

The term *material hourglassing* will be used to describe artificial instabilities that arise due to material nonlinearities, usually accompanied by strain softening, that is, horizontal tangents in the stress strain relation. These phenomena

are closely related to (global) physical instabilities as well as (local) material instability of the underlying constitutive model, see for example, Petryk³⁰ or the descriptive discussion in Chen and Baker.³¹ In other words, problems that suffer from material hourglass formation are also susceptible to physical material-induced instabilities and an hourglass study requires consideration of both phenomena.

Material hourglassing, as opposed to geometric hourglassing, is driven by a negative material stiffness. In the context of EAS elements it was shown by Armero¹⁶ that the strain enhancement that eliminates volumetric locking is responsible for this type of numerical instability. Typical cases in which material hourglassing is observed for EAS elements are inelastic problems, such as the necking simulations of stretched specimens.^{32,33} However, also elastic simulations under certain tensile stress conditions can exhibit material hourglassing, as shown in Reese et al.⁸ (Sec. 4.5.2). Besides EAS elements, displacement-pressure type formulations (e.g., Q1/P0) may also suffer from material hourglassing, although less pronounced, see for example, References 12,34 or Auricchio et al.^{19,35} In this context it was shown by Schröder et al.²⁴ that numerical stability of two-field formulations, with an independent pressure field as additional unknown, can depend on the choice of the penalty function that weakly enforces the volume constraint, whereas the classical three-field formulation of Simo et al.³⁶ is more robust. Interestingly, the combined formulation of Q1/P0 and EAS of Reference 16 shows promising results for 2D problems but fails in 3D simulations, as recently shown by Hille et al.³⁷

Resolving the issue of material hourglassing remains rather laborious and many approaches involve a reintroduction of locking. In order to alleviate material hourglassing, Simo et al.³² proposed higher order integration. This, however, appears to be a pyrrhic victory, because the higher order integration introduces certain locking effects that only appear in nonlinear problems. These higher order, nonlinear locking phenomena have been detected only recently by Willmann et al.³⁸ In fact, it is this nonlinear locking phenomenon that produces the stabilizing effect.

With a similar motivation Glaser and Armero²¹ proposed to stabilize EAS elements via a variational control term, penalizing the EAS-induced volumetric energy, see also References 39,40. This typically requires a proper choice for the penalty factor, that is, a balance between the numerical model being too stiff (reintroducing locking) and too flexible (hourglassing). An ad hoc stabilization was proposed by Reese⁴¹ by enforcing a positive definite tangent and thus ensuring a positive hourglass (stabilization) stiffness. Typical drawbacks of this approach are its parameter dependency as well as loss of accuracy in bending dominated problems. Similar to the case of geometric hourglassing in Reference 23 material hourglassing is avoided via a linear elastic description of the higher order stiffness.

Ongoing research activities in the field indicate that, despite the presence of individual solutions, a general solution or understanding is still lacking. This point of view is strengthened by the authors' observation that the aforementioned formulations have barely entered commercial finite element codes. Therefore, an improvement of existing established formulations is a primary motivation in the present contribution.

A further essential difficulty in the analysis of numerical instabilities coming along with geometric and material hourglassing is that they are inevitably connected to deformation states that are also potentially prone to physical instabilities. Thus, getting a clear view on whether or not hourglassing is present, one always has to cope with the physical instability problem, see Auricchio et al.³⁵ It is therefore essential to consider both effects in a proper analysis of nonlinear finite elements. The requirements on proper element design are twofold: (i) physical instabilities should be captured accurately, that is, good convergence towards the correct critical points with mesh refinement, which is achieved by a consistent finite element formulation as well as a locking-free response; (ii) artificial instabilities should be excluded, that is, a singular stiffness matrix should exclusively be related to a physical instability.

The remainder of the paper is structured as follows: Section 2 aims to show, in a simplified manner, how locking-free element formulations influence the geometric stiffness and how this triggers numerical instabilities. Section 3 reviews some popular element formulations from literature. Closely related to the work of Armero,¹⁶ the modal analysis in Section 3.4 provides some additional insights in terms of geometric and material hourglassing. The core contribution of this work consists in the stabilization concept to avoid geometric hourglassing in Section 4 as well as the in-depth analysis of the benchmark setup proposed in Section 5. Finally, a collection of elements is tested for some standard benchmarks in Section 6.

2 | PHYSICAL AND ARTIFICIAL BUCKLING: SOME SIMPLE CONSIDERATIONS

2.1 | Element stability

With the aim of explaining how unlocking schemes have an influence on the geometric stiffness and trigger artificial buckling, we focus on the stability properties of a two-dimensional $L_1^e \times L_2^e$ rectangular incompatible mode element* from

Wilson et al.⁴² The element is under plane strain conditions with out-of-plane unit thickness, furthermore kinematic constraints are enforced such that the displacements are zero at the element centroid. A homogeneous uniaxial stress state $\sigma_{22} = -\gamma p$ is applied, see Figure 1A, where p is a reference (unit) load and γ is a load parameter, indicating the load magnitude.

To gain some mechanical insights on the element’s stability properties, we consider a classical pre-buckling analysis⁴³

$$(\mathbf{K}_e + \gamma_c \mathbf{K}_g^{\text{LIN}}) \Phi = \mathbf{0} \quad \text{with } \Phi \neq \mathbf{0}. \tag{1}$$

Here \mathbf{K}_e is the linear elastic stiffness matrix and $\mathbf{K}_g^{\text{LIN}}$ is the linearized geometric stiffness matrix, defined as $\mathbf{K}_g^{\text{LIN}} = \frac{d}{d\gamma} \mathbf{K}_g|_{\gamma=0}$, where \mathbf{K}_g is the fully nonlinear geometric stiffness matrix. The smallest positive eigenvalue of this generalized eigenvalue problem provides an estimate for the critical load factor γ_c and the corresponding eigenvector Φ indicates the buckling mode.

With natural element coordinates $(\xi, \eta) \in \Omega_{\text{ref}} = [-1, 1]^2$ and taking into account the aforementioned geometric constraints, a general displacement field within the element can be expressed as

$$\mathbf{u} = \mathbf{u}^c + \tilde{\mathbf{u}} = \underbrace{\frac{1}{2} \begin{bmatrix} c_1 \xi + c_3 \eta + c_5 \xi \eta \\ c_2 \eta + c_4 \xi + c_6 \xi \eta \end{bmatrix}}_{\text{compatible}} + \underbrace{\frac{1}{4} \begin{bmatrix} c_7 (\eta^2 - 1) \\ c_8 (\xi^2 - 1) \end{bmatrix}}_{\text{incompatible}}, \tag{2}$$

where parameters c_{1-6} represent the *compatible* displacement modes and c_{7-8} are the *incompatible* modes, introduced to eliminate shear locking.

In the following, we study the properties of stiffness matrices referring to c_{1-8} as generalized degrees of freedom. Using a standard isoparametric mapping $\Omega_{\text{ref}} \rightarrow \Omega$, the linear elastic stiffness matrix for an isotropic elastic material with Young’s modulus E , shear modulus $G = E/2$ (implying that Poisson’s ratio is zero) and element aspect ratio $r_e = L_1^e/L_2^e$ is given as

$$\mathbf{K}_e = [K_e^{AB}] = \begin{bmatrix} \mathbf{K}_e^0 & \mathbf{0} \\ \mathbf{0} & \mathbf{K}_e^1 \end{bmatrix} \tag{3}$$

with

$$\mathbf{K}_e^0 = \begin{bmatrix} \frac{E}{r_e} & 0 & 0 & 0 \\ 0 & Er_e & 0 & 0 \\ 0 & 0 & Gr_e & G \\ 0 & 0 & G & \frac{G}{r_e} \end{bmatrix} \quad \text{and} \quad \mathbf{K}_e^1 = \frac{1}{3} \begin{bmatrix} \frac{E}{r_e} + Gr_e & 0 & 0 & G \\ 0 & Er_e + \frac{G}{r_e} & G & 0 \\ 0 & G & Gr_e & 0 \\ G & 0 & 0 & \frac{G}{r_e} \end{bmatrix}. \tag{4}$$

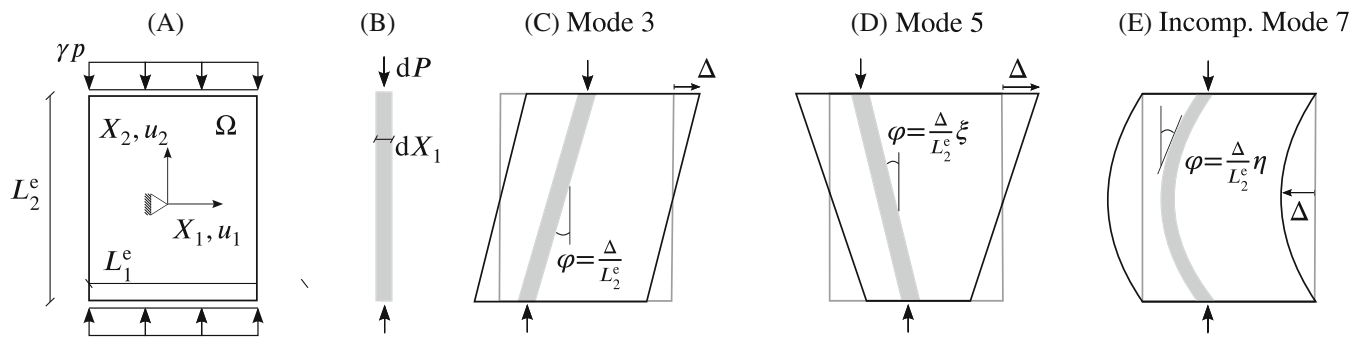


FIGURE 1 (A) Model problem and (B) infinitesimal line segment $dX_1 \times L_2^e$ and load $dP = \gamma p dX_1$. (C)–(E) Modes where the P - Δ -effect contributes to the geometric stiffness via integration of $(\partial\varphi/\partial\Delta)^2 dP$ over the element domain

Here, the upper indices A, B refer to the modal degrees of freedom c_A and c_B . The first part \mathbf{K}_e^0 contains the three constant strain modes, required for consistency, and a rigid body rotation. The second part \mathbf{K}_e^1 represents the stiffness related to the non-constant strain modes c_{5-8} . The issue of in-plane shear locking is reflected by the shear terms in $K_e^{55} = E/(3r_e) + Gr_e/3$ and $K_e^{66} = Er_e/3 + G/(3r_e)$, which become infinite for the limit cases $r_e \rightarrow \infty$ and $r_e \rightarrow 0$, respectively. However, thanks to the incompatible modes this pathology is removed. For more details we refer to Appendix A. We focus now on the implications of ansatz (2) on the geometric stiffness matrix, which turns out to be a diagonal matrix

$$\mathbf{K}_g = \gamma \mathbf{K}_g^{\text{LIN}} = \gamma \cdot \text{diag} \left(0, \underline{-pr_e}, \underline{-pr_e}, 0, \underline{-\frac{pr_e}{3}}, \underline{-\frac{pr_e}{3}}, \underline{-\frac{pr_e}{3}}, 0 \right). \quad (5)$$

Here, the essential trigger mechanism for geometric instabilities are the three underlined terms. They are related to a phenomenon denoted as ‘‘P- Δ -effect’’ in structural mechanics.[†] It is a destabilizing stiffness that emanates from a change of lever arms of axial forces due to lateral displacements in axially compressed structures. To specify this further, computation of the entries of the geometric stiffness matrix can be boiled down to (no summation)

$$K_g^{AA} = \int_{\Omega} \frac{\partial^2}{\partial c_A^2} \frac{1}{2} (\mathbf{H}^T \mathbf{H}) : \boldsymbol{\sigma} \, dA = \int_{\Omega} \frac{\partial^2}{\partial c_A^2} \frac{1}{2} (H_{12}^2 + H_{22}^2) \cdot \sigma_{22} \, dA, \quad (6)$$

with the displacement gradient $\mathbf{H} = \text{Grad} \mathbf{u}$. Herein, the stiffness contributions due to

$$H_{12}^2 = \left(\frac{\partial u_1}{\partial X_2} \right)^2 = \frac{(c_3 + c_5 \xi + c_7 \eta)^2}{(L_2^e)^2} \quad (7)$$

are associated with the P- Δ -terms. A geometric illustration of the involved element strain modes 3, 5 and 7 is given in Figure 1B–E. Next, the degrees of freedom c_7 and c_8 , associated with the incompatible modes, are eliminated on element level via static condensation. This provides a reduced stiffness matrix, which is given in Appendix A. For small ratios of σ_{22}/E the reduced stiffness matrix can be approximated as

$$\mathbf{K}_{\text{red}}^1 \approx \begin{bmatrix} \frac{E}{3r_e} & 0 \\ 0 & \frac{Er_e}{3} \end{bmatrix} + \begin{bmatrix} \frac{r_e}{3} \sigma_{22} & 0 \\ 0 & \frac{r_e^2+1}{3r_e} \sigma_{22} \end{bmatrix} \quad (8)$$

and we will work with this approximation in the following.

With these preliminary considerations we now focus on critical load factors γ_c that are solutions of the eigenvalue problem (1). For the part of the stiffness matrix associated with the constant strain modes, the only instability on element level is the rigid body rotation with $\gamma_c = 0$. The geometric term $K_g^{33} = -\gamma pr_e$ is crucial for consistency, that is, providing the correct (physical) stability behavior with mesh refinement. The stability properties of the higher modes are directly linked to two different geometric hourglass phenomena:

1. For a large aspect ratio $r_e \gg 1$ geometric hourglassing is likely to occur in the shape of mode 5. It is triggered by the negative geometric stiffness $K_g^{55} = -\gamma pr_e/3$ associated with this mode. With the shear locking-free reduced stiffness (after static condensation) we obtain

$$K_{\text{red}}^{55} = \frac{E}{3r_e} - \frac{\gamma_c pr_e}{3} = 0 \quad \rightarrow \quad \boxed{\gamma_c = \frac{E}{pr_e^2}} \quad (9)$$

This value represents an approximation of the critical load factor that yields the ‘‘classical’’ geometric hourglassing of mode 5.

2. On the other side, for small aspect ratios $r_e \ll 1$ ($L_1^e \ll L_2^e$), the geometric term $K_g^{77} = -\gamma pr_e/3$, related to the incompatible mode 7 triggers an instability of mode 6. With the approximated reduced stiffness (after static condensation, cf. Appendix A.1) we obtain

$$K_{\text{red}}^{66} \approx \frac{Er_e}{3} - \frac{\gamma_c p r_e}{3} - \frac{\gamma_c p}{3r_e} = 0 \quad \rightarrow \quad \boxed{\gamma_c = \frac{Er_e^2}{p(1+r_e^2)} \approx \frac{E}{p} r_e^2} \quad (10)$$

This represents the value that triggers hourglassing of mode 6 and resembles a (quadratic) Ritz approximation of the Euler buckling load $p_c^{\text{Euler}} = \pi^2 Er_e^2 / 12 \approx 0.82 Er_e^2$ of a beam pinned at both ends. In literature it is frequently concluded that this mode is “physically correct”. However, this is refuted within the next subsection.

A similar analysis, based on small strain theory, can also be found in the work of Sussman and Bathe.¹⁵ It is shown in the next section that both element instabilities (mode 5 and 6) can spoil the real, physical instability properties and yield undesired hourglass patterns.

An alternative formulation, denoted as Q1/HT4 (cf. Section 3.3.3), relies on the “transposed Wilson modes” proposed in References 20,21. This enhancement cannot be derived from an incompatible displacement field. It can be incorporated within the EAS framework via the strain enhancement $\tilde{\mathbf{H}} = \text{Grad} \tilde{\mathbf{u}}^T$. By a similar analysis as above (cf. Appendix A.2) it can be shown that the reduced hourglass stiffness then reads

$$K_{\text{red}}^{55} = \frac{E}{3r_e} - \frac{\gamma p r_e}{3} + \underbrace{\frac{\gamma p r_e}{3}}_{\text{EAS term}} = \frac{E}{3r_e} \quad \text{and} \quad K_{\text{red}}^{66} = \frac{Er_e}{3} - \frac{\gamma p r_e}{3}, \quad (11)$$

effectively excluding all critical geometric stiffness terms and thus avoiding geometric hourglassing, while maintaining the favorable locking-free response. It provides a clear mechanical explanation why the element is free of geometric hourglassing. However, this approach is not applicable to other element formulations, such as the Q1/E4 based on an enhancement of the Green-Lagrange strain (cf. Section 3.3.2).

2.2 | Patch stability

Besides the deformation state, whether or not geometric hourglassing occurs within a patch of elements depends mainly on r_e as well as on the displacement boundary conditions. To exclude any influence of the latter, we consider again the minimally constrained problem sketched in Figure 1A but with an assembled patch of elements. Now, we have to differentiate between the element’s aspect ratio r_e and the block’s aspect ratio denoted as $r = L_1/L_2$, with L_i being the length of the block in direction X_i . Next, we compare the results of a fully nonlinear finite element analysis with a compressible Neo-Hookean material ($E = 1000$, $\nu = 0$) with the estimates of the preceding section.

Figure 2 shows the undeformed reference mesh (grey) as well as the first three buckling modes $\Phi^{(j)}$ superimposed on the deformed configuration for various discretizations of a short block, (A)–(C), and a tall block, (D)–(F). Each buckling mode corresponds to the eigenvector associated with a zero eigenvalue[‡] of the stiffness matrix emanating from the primary path (uniaxial homogeneous compression). Furthermore, the load values $\gamma_c^{(j)}$, related to the critical points in increasing order, as well as the hourglass estimates (9) and (10) are listed in Table 1.

Geometric hourglassing occurs when the critical load of a single element is reached. Depending on the global (physical) stability behavior, this can occur for the first critical point (e.g., $r = 10$, $r_e = 20$ or $r = 1/10$, $r_e = 1/20$ in Table 1) or for higher ones (e.g., Figure 2B,C,E,F), in case physical buckling is initially dominant.

The estimates (9) and (10) are only reasonable for stiff structures, for which the pre-buckling behavior is approximately linear. Thus, for $r_e \approx 1$, these predictions become a poor approximation and a large strain analysis is required. Nevertheless, the principal mechanism that triggers hourglassing remains the same.

2.3 | Summary

The presented results can be summarized as follows:

- Geometric hourglassing of mode 5 is triggered by the geometric stiffness originating from the same *compatible* mode 5, that is, K_g^{55} in Equation (5). This is especially pronounced for large element aspect ratios $r_e \gg 1$, see Equation (9).

TABLE 1 Critical load factor γ_c based on the minimum of estimate (9) and (10) and the j^{th} critical load factor $\gamma_c^{(j)}$ of the fully nonlinear finite element analysis with different structured $n_{\text{ele}}^{X_1} \times n_{\text{ele}}^{X_2}$ meshes

Mesh	$r = r_e$	γ_c	$\gamma_c^{(1)}$	$\gamma_c^{(2)}$	$\gamma_c^{(3)}$
Short block $r = 10$					
1 × 1	10	10	9.9	—	—
2 × 2	10	10	9.9	9.9*	38.37*
4 × 4	10	10	8.56	9.9*	14.92*
2 × 4	20	2.5	2.49*	3.77*	9.86
4 × 2	5	40	8.58	38.4*	38.4
40 × 4	1	—	8.14	31.55	67.05
Tall block $r = 1/10$					
1 × 1	1/10	9.9	9.61	—	—
2 × 2	1/10	9.9	9.61	9.61*	34.42*
4 × 4	1/10	9.9	8.34	9.61*	14.28*
2 × 4	1/5	38.46	8.37	34.42*	34.42
4 × 2	1/20	2.49	2.48*	3.73*	9.58
4 × 40	1	—	7.95	28.85	56.12

Note: Values marked with * are afflicted with geometric hourglassing.

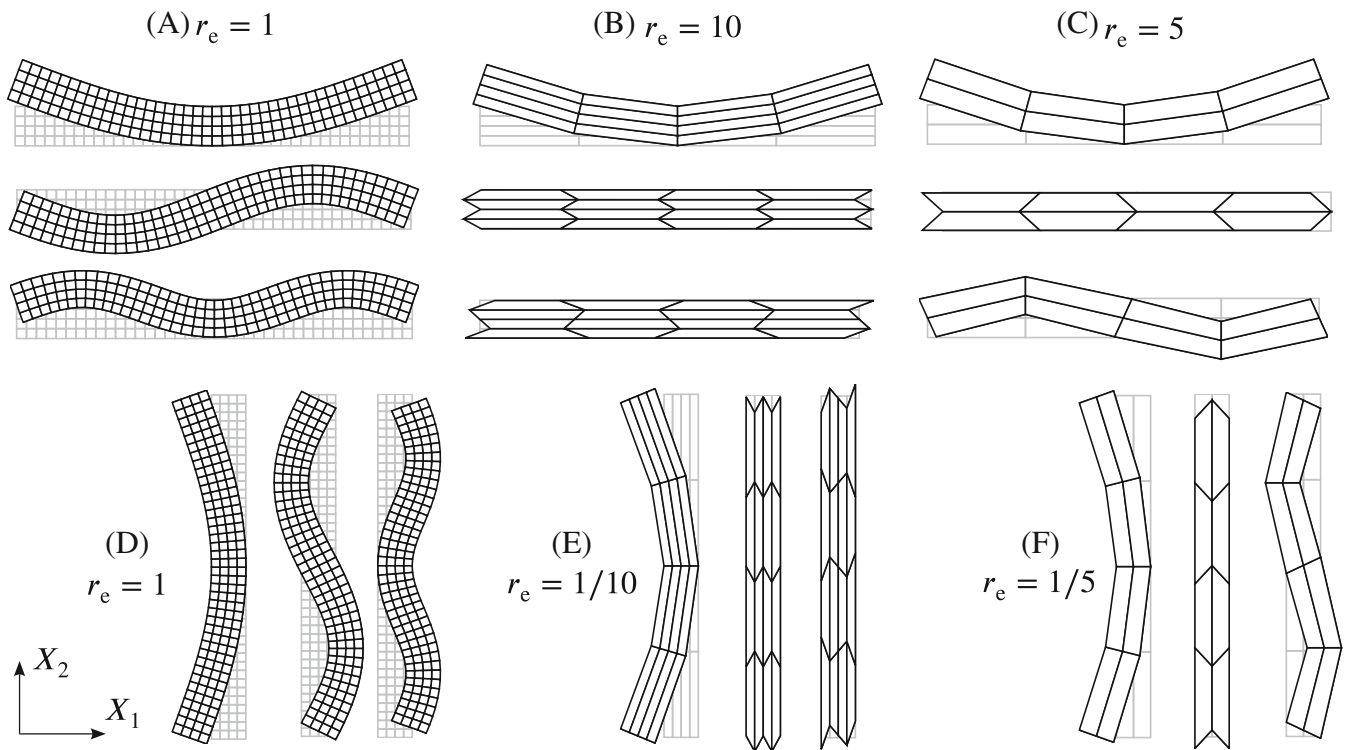


FIGURE 2 Physical or artificial buckling modes for a discretized uniaxial prestressed block, compare Figure 1A, with aspect ratio of $r = 10$ (top) and $r = 1/10$ (bottom). The first three modes are shown for each configuration

- Geometric hourglassing of mode 6 is triggered by the geometric stiffness originating from the *incompatible* mode 7, that is, K_g^{77} in Equation (5). This is especially pronounced for small element aspect ratios $r_e \ll 1$, see Equation (10).
- Both estimates (9) and (10) are a good approximation of the critical load associated with the artificial buckling modes in the small strain regime, that is, for the limit cases of r_e .
- The strain enhancement of the Q1/HT4, based on the “transposed Wilson modes”, modifies the geometric stiffness such that the destabilizing geometric terms cancel and consequently geometric hourglassing is avoided.

In view of the remainder of the work we point out that a straightforward solution to avoid geometric hourglassing is to skip the responsible geometric stiffness terms. A novel and economic way to achieve this is the core of Section 4.

3 | A FAMILY OF QUADRILATERAL FINITE ELEMENTS

3.1 | Continuum mechanics

Let us briefly recall some basic notation and equations that are a prerequisite for the finite elasticity problems in the subsequent sections. The main kinematic and constitutive relations are summarized in Table 2, see textbooks.^{11,44} Throughout the remainder of this work, only elasto-static plane strain problems are studied.

We consider a problem with displacement-controlled loading, governed by the balance of linear momentum

$$\text{Div} \mathbf{P} = 0 \quad \text{in } \mathcal{B}, \quad (12)$$

with prescribed displacements $\mathbf{u} = \hat{\mathbf{u}}$ on the respective boundary. This implies a stationary elastic potential

$$\Pi[\mathbf{u}] = \int_{\mathcal{B}} W(\mathbf{E}) \, dA = \int_{\mathcal{B}} \overline{W}(\mathbf{F}) \, dA \Rightarrow \text{stat.}, \quad (13)$$

giving rise to the weak form

$$\delta \Pi[\mathbf{u}, \delta \mathbf{u}] := \delta \mathbf{u} \cdot \Pi_{,\mathbf{u}} = \int_{\mathcal{B}} \delta \mathbf{E}(\mathbf{u}, \delta \mathbf{u}) : \mathbf{S}(\mathbf{u}) \, dA = \int_{\mathcal{B}} \delta \mathbf{F}(\delta \mathbf{u}) : \mathbf{P}(\mathbf{u}) \, dA = 0, \quad (14)$$

with admissible variations $\delta \mathbf{u}$. The comma denotes a partial derivative with respect to \mathbf{u} . Linearization of (12) provides the incremental expression

$$\begin{aligned} \Delta \delta \Pi[\mathbf{u}, \delta \mathbf{u}, \Delta \mathbf{u}] &:= \delta \mathbf{u} \cdot \Pi_{,\mathbf{u}\mathbf{u}} \Delta \mathbf{u} = \int_{\mathcal{B}} \{ \delta \mathbf{E}(\mathbf{u}, \delta \mathbf{u}) : \mathbb{C}(\mathbf{u}) : \Delta \mathbf{E}(\mathbf{u}, \Delta \mathbf{u}) + \Delta \delta \mathbf{E} : \mathbf{S}(\mathbf{u}) \} \, dA \\ &= \int_{\mathcal{B}} \delta \mathbf{F}(\delta \mathbf{u}) : \mathbb{A}(\mathbf{u}) : \Delta \mathbf{F}(\Delta \mathbf{u}) \, dA, \end{aligned} \quad (15)$$

TABLE 2 Basic variables and notation

\mathcal{B}	Material configuration	$\varphi(\mathcal{B})$	Spatial configuration
$\mathbf{X} \in \mathcal{B}$	Material points	$\mathbf{x} = \varphi(\mathbf{X})$	Spatial points / deformation map
$\mathbf{F} = \text{Grad} \varphi$	Deformation gradient	\mathbf{u}	Displacement field
$J = \det \mathbf{F}$	Jacobian (volume change)	$\mathbf{H} = \text{Grad} \mathbf{u}$	Displacement gradient
$\mathbf{F}^T \mathbf{F}$	Right Cauchy-Green strain	$\mathbf{E} = \frac{1}{2}(\mathbf{C} - \mathbf{1})$	Green-Lagrange strain
$W(\mathbf{E}), \overline{W}(\mathbf{F})$	Strain energy functions	λ_1, λ_2	Principle stretches
$\mathbf{S} = \partial_{\mathbf{E}} W$	Second Piola-Kirchhoff stress	$\mathbf{P} = \partial_{\mathbf{F}} \overline{W}$	First Piola-Kirchhoff stress
$\mathbb{C} = \partial_{\mathbf{E}\mathbf{E}} W$	Elasticity tensor related to conjugate pair (\mathbf{S}, \mathbf{E})	$\mathbb{A} = \partial_{\mathbf{F}\mathbf{F}} \overline{W}$	Elasticity tensor related to conjugate pair (\mathbf{P}, \mathbf{F})
Ω	Element area (material)	\mathbf{d}	Nodal element disp. vector
$\mathbf{k}^{b\sharp}$	Element stiffness matrix related to DOFs b and \sharp	\mathbf{r}^b	Element residual vector related to DOF b

required for definition of the tangent stiffness matrix. Here $\Delta \mathbf{u}$ denotes the incremental displacement field. The strain variations and increments are given by

$$\delta \mathbf{H} = \text{Grad} \delta \mathbf{u}, \quad \Delta \mathbf{H} = \text{Grad} \Delta \mathbf{u}, \quad \delta \mathbf{E} = \text{sym}(\mathbf{F}^T \delta \mathbf{H}), \quad \Delta \delta \mathbf{E} = \text{sym}(\Delta \mathbf{H}^T \delta \mathbf{H}). \quad (16)$$

These equations are the variational basis for the subsequent finite element formulations. For standard displacement based finite elements corresponding formulations described within a *total Lagrangian setting* (\mathbf{S}, \mathbf{E}) or a *two-point setting* (\mathbf{P}, \mathbf{F}) are identical. However, for EAS formulations it has various implications, which will be discussed in the following.

3.2 | Displacement formulation (Qp-elements)

Let us consider a standard finite element procedure with isoparametric plane quadrilateral Qp-elements with bilinear shape functions for $p = 1$, biquadratic shape functions for $p = 2$, and so forth. The geometry and displacement approximation for a generic element e are given as

$$\mathbf{X}^h = \sum_{A=1}^{n_{\text{no}}} N^A \mathbf{X}^A \quad \text{and} \quad \{\mathbf{u}, \delta \mathbf{u}, \Delta \mathbf{u}\}^h = \sum_{A=1}^{n_{\text{no}}} N^A \{\mathbf{d}^A, \delta \mathbf{d}^A, \Delta \mathbf{d}^A\}, \quad (17)$$

where n_{no} denotes the number of element nodes, $N^A(\xi, \eta)$ is the Lagrangian shape function of node A defined on the reference element $\Omega_{\text{ref}} = [-1, 1]^2$ and $\{\mathbf{d}^A, \delta \mathbf{d}^A, \Delta \mathbf{d}^A\}$ are the actual, virtual and incremental nodal displacements. The basis of an incremental-iterative finite element procedure is the linearized discrete representation of the weak form (12)

$$\mathbf{K} \Delta \mathbf{D} = -\mathbf{R} \quad \text{with} \quad (\mathbf{K}, \mathbf{R}, \mathcal{B}^h) = \bigcup_{e=1}^{n_{\text{ele}}} (\mathbf{k}_e^{\text{dd}}, \mathbf{r}_e^{\text{d}}, \Omega_e), \quad (18)$$

where standard assembly procedures of the element stiffness matrix and residual vector are used. Here n_{ele} denotes the total number of elements and $\Delta \mathbf{D}$ the global displacement vector. For ease of readability, we will skip the indices e and h in the following. If not otherwise stated, the expressions always refer to the discretized variables of one generic element. Tensor and matrix notation are not further distinguished and should become clear from the context.

In view of the following developments we introduce the *compatible Green-Lagrange strain* of a generic element as

$$\mathbf{E}^c(\mathbf{d}) := \frac{1}{2} \left(\mathbf{H}^{\text{cT}} + \mathbf{H}^c + \mathbf{H}^{\text{cT}} \mathbf{H}^c \right), \quad (19)$$

with element displacement vector \mathbf{d} , based on the compatible displacement gradient $\mathbf{H}^c = \text{Grad} \mathbf{u}$ derived from (15)₂. Related to (12) and (13) we obtain the internal force vector

$$\mathbf{r}^{\text{d}} := \Pi_{,\mathbf{d}} = \int_{\Omega} \mathbf{E}_{,\mathbf{d}}^c : \mathbf{S} \, dA \quad (20)$$

and the element stiffness matrix

$$\mathbf{k}^{\text{dd}} := \Pi_{,\mathbf{d}\mathbf{d}} = \underbrace{\int_{\Omega} \mathbf{E}_{,\mathbf{d}}^c : \mathbb{C} : \mathbf{E}_{,\mathbf{d}}^c \, dA}_{\mathbf{k}_m^{\text{dd}}} + \underbrace{\int_{\Omega} \mathbf{E}_{,\mathbf{d}\mathbf{d}}^c : \mathbf{S} \, dA}_{\mathbf{k}_g^{\text{dd}}}. \quad (21)$$

Here, we employ a split of the stiffness matrix into a *material* part \mathbf{k}_m^{dd} and a *geometric* part \mathbf{k}_g^{dd} . In view of what comes next, we emphasize that the geometric stiffness depends only on the nonlinear (quadratic in \mathbf{d}) part $\mathbf{H}^{\text{cT}} \mathbf{H}^c$ of the strain expression (17), see also the incremental expression (14)₄.

For the actual implementation it is practical to represent (18) and (19) in Voigt notation as

$$\mathbf{r}^{\text{d}} = \int_{\Omega} \mathbf{B}^T \mathbf{S} \, dA \quad \text{and} \quad \mathbf{k}^{\text{dd}} = \int_{\Omega} \mathbf{B}^T \mathbf{C}(\mathbf{E}^c) \mathbf{B} \, dA + \int_{\Omega} \mathbb{G}^{\text{dd}}(\mathbf{E}^c, \mathbf{S}) \, dA, \quad (22)$$

with the incremental strain-displacement operator

$$\mathbf{B} := \begin{bmatrix} E_{11}^c & E_{22}^c & 2E_{12}^c \end{bmatrix}_{,\mathbf{d}}^T \quad (23)$$

and the geometric operator

$$\mathbb{G}^{\text{dd}}(\mathbf{E}^c, \mathbf{S}) = \left[(G^{\text{dd}} \delta_{jk})^{AB} \right] := (H_{iI} H_{iJ})_{,d^A d_k^B} S_{IJ} = N_{,I}^A S_{IJ} N_{,J}^B \delta_{jk}^{AB}. \quad (24)$$

Here, upper indices A, B refer to the element nodes and lower indices i, j, \dots and I, J, \dots to the spatial and material coordinates, respectively.

3.3 | Enhanced assumed strain formulations

3.3.1 | General concept

A well established class of finite elements for nonlinear problems are enhanced assumed strain (EAS) elements, proposed by Simo's landmark contributions.^{12,13} The EAS method is a variationally consistent version of the method of incompatible modes, developed earlier to avoid various locking phenomena. The principal idea is to enrich the compatible displacement based strain by an enhanced assumed strain field defined through internal (element-wise defined) parameters α . Starting point is a three-field functional, which, after enforcing a certain orthogonality condition, yields a discrete representation of a two-field elastic potential,

$$\tilde{\Pi}[\mathbf{d}, \alpha] = \int_{\Omega} W[\mathbf{E}(\mathbf{d}, \alpha)] \, dA. \quad (25)$$

The appealing features are its simplicity as well as the strain driven format, which enables a broad scope of applications concerning the material model. The chosen ansatz functions for the enhanced strain crucially influence the (locking-) behavior of the element. Moreover, for the geometrically nonlinear case the type of strain measure that is subject to enhancement is important, particularly with respect to hourglassing. This point will be further highlighted in the next sections.

Based on (23) the discrete system of incremental element equations reads

$$\begin{bmatrix} \mathbf{k}^{\text{dd}} & \mathbf{k}^{\text{d}\alpha} \\ \mathbf{k}^{\alpha\text{d}} & \mathbf{k}^{\alpha\alpha} \end{bmatrix} \begin{bmatrix} \Delta \mathbf{d} \\ \Delta \alpha \end{bmatrix} = - \begin{bmatrix} \mathbf{r}^{\text{d}} \\ \mathbf{r}^{\alpha} \end{bmatrix}, \quad (26)$$

where \mathbf{r}^{d} and \mathbf{k}^{dd} are obtained by replacing Π with $\tilde{\Pi}$ in (18) and (19) respectively. The remaining contributions are

$$\mathbf{r}^{\alpha} := \tilde{\Pi}_{,\alpha} = \int_{\Omega} \mathbf{E}_{,\alpha} : \mathbf{S} \, dA = 0, \quad (27)$$

$$\mathbf{k}^{\alpha\alpha} := \tilde{\Pi}_{,\alpha\alpha} = \underbrace{\int_{\Omega} \mathbf{E}_{,\alpha} : \mathbb{C} : \mathbf{E}_{,\alpha} \, dA}_{\mathbf{k}_m^{\alpha\alpha}} + \underbrace{\int_{\Omega} \mathbf{E}_{,\alpha\alpha} : \mathbf{S} \, dA}_{\mathbf{k}_g^{\alpha\alpha}}, \quad (28)$$

$$\mathbf{k}^{\alpha\text{d}} := \tilde{\Pi}_{,\alpha\text{d}} = \underbrace{\int_{\Omega} \mathbf{E}_{,\alpha} : \mathbb{C} : \mathbf{E}_{,\text{d}} \, dA}_{\mathbf{K}_m^{\alpha\text{d}}} + \underbrace{\int_{\Omega} \mathbf{E}_{,\alpha\text{d}} : \mathbf{S} \, dA}_{\mathbf{k}_g^{\alpha\text{d}}} = (\mathbf{k}^{\text{d}\alpha})^T. \quad (29)$$

Since the enhanced strain parameters are defined on element level they are usually eliminated via static condensation

$$\underbrace{(\mathbf{k}^{\text{dd}} - \mathbf{k}^{\text{d}\alpha} (\mathbf{k}^{\alpha\alpha})^{-1} \mathbf{k}^{\alpha\text{d}})}_{\mathbf{k}_{\text{red}}} \Delta \mathbf{d} = - \underbrace{(\mathbf{r}^{\text{d}} - \mathbf{k}^{\text{d}\alpha} (\mathbf{k}^{\alpha\alpha})^{-1} \mathbf{r}^{\alpha})}_{\mathbf{r}_{\text{red}}}, \quad (30)$$

with \mathbf{k}_{red} and \mathbf{r}_{red} being the reduced element stiffness matrix and element residual vector.

A representation in matrix notation is obtained in analogy to the preceding section, with incremental strain-enhancement operator $\tilde{\mathbf{B}} = \mathbf{E}_{,\alpha}^T$ and, similar to (22), geometric operators $\mathbb{G}^{aa}(\mathbf{E}, \mathbf{S})$ and $\mathbb{G}^{ad}(\mathbf{E}, \mathbf{S})$.

3.3.2 | Enhancement of Green-Lagrange strain (Qp/En)

The first class of EAS elements considered here is based on an additive enhancement of the compatible Green-Lagrange strain tensor (17)

$$\mathbf{E}(\mathbf{d}, \boldsymbol{\alpha}) = \mathbf{E}^c(\mathbf{d}) + \tilde{\mathbf{E}}(\boldsymbol{\alpha}), \quad (31)$$

where $\tilde{\mathbf{E}} = \frac{\det(\mathbf{J}_0)}{\det(\mathbf{J})} \mathbf{J}_0^{-T} \tilde{\mathbf{E}}^{\text{ref}} \mathbf{J}_0^{-1}$ denotes the enhanced strain⁸ and $\tilde{\mathbf{E}}^{\text{ref}}$ is a linear function of $\boldsymbol{\alpha}$. Elements based on this concept are particularly popular for the membrane part of shell elements^{45,46} as well as for three-dimensional brick elements.⁴⁷

The variational basis may be derived by inserting (29) into a total Lagrangian three-field Hu-Washizu type functional

$$\Pi_{\text{SE}}[\mathbf{d}, \boldsymbol{\alpha}, \mathbf{S}^*] = \int_{\Omega} (W(\mathbf{E}^c + \tilde{\mathbf{E}}) - \underline{\mathbf{S}^*} : \tilde{\mathbf{E}}) \, dA \quad (32)$$

and exploiting the orthogonality condition (cf. References 13,45) between the independent stress \mathbf{S}^* and the enhanced strain field $\tilde{\mathbf{E}}$, which removes the underlined term in (30) and thus recovers (23).

An interpretation of the strain enhancement (29) via an incompatible displacement ansatz is only possible for the geometrically linear case and from (26) to (27) it becomes clear that the geometric part of the stiffness matrix is not influenced, since $\mathbf{E}_{,d\alpha} = \mathbf{0}$ and $\mathbf{E}_{,\alpha\alpha} = \mathbf{0}$. Thus, geometric hourglassing is fully driven by the geometric stiffness in Equation (19), that is, by the compatible displacement degrees of freedom.

A popular formulation is the Q1/E4 element, defined by the enhancement

$$\tilde{\mathbf{E}}^{\text{ref}} = \begin{bmatrix} \xi \alpha_1 & \xi \alpha_3 + \eta \alpha_4 \\ \xi \alpha_3 + \eta \alpha_4 & \eta \alpha_2 \end{bmatrix}. \quad (33)$$

For undistorted elements, volumetric locking and shear locking are fully removed by this ansatz. Alternative formulations that only handle one of the two locking issues are denoted as Q1/E2n (using only α_1, α_2) and Q1/E2s (using only α_3, α_4) in this paper. Another element that will be considered in the subsequent analysis is the Q2/E11 element proposed by Bischoff and Ramm.⁴⁶ This element formulation avoids volumetric locking and shear locking, present in the displacement based nine-noded Q2 with the strain enhancement

$$\begin{aligned} \tilde{E}_{11}^{\text{ref}} &= \alpha_1(1 - 3\xi^2) + \alpha_2(\eta - 3\xi^2\eta) + \alpha_3(\eta^2 - 3\xi^2\eta^2), \\ \tilde{E}_{22}^{\text{ref}} &= \alpha_4(1 - 3\eta^2) + \alpha_5(\xi - 3\xi\eta^2) + \alpha_6(\xi^2 - 3\xi^2\eta^2), \\ \tilde{E}_{12}^{\text{ref}} &= \alpha_7(1 - 3\xi^2) + \alpha_8(1 - 3\eta^2) + \alpha_9(\eta - 3\xi^2\eta) + \alpha_{10}(\xi - 3\xi\eta^2) + \alpha_{11}(1 - 3(\xi^2 + \eta^2) + 9\xi^2\eta^2), \end{aligned} \quad (34)$$

see also Section 3.3 in Reference 46.

3.3.3 | Enhancement of displacement gradient (Q1/H4 and Q1/HT4)

The second element class that we consider is the classical nonlinear EAS formulation by Simo and Armero.¹² It can be formulated via an additive enhancement of the compatible displacement gradient as

$$\mathbf{H}(\mathbf{d}, \boldsymbol{\alpha}) = \mathbf{H}^c(\mathbf{d}) + \tilde{\mathbf{H}}(\boldsymbol{\alpha}), \quad (35)$$

where $\tilde{\mathbf{H}} = \frac{\det(\mathbf{J}_0)}{\det(\mathbf{J})} \mathbf{J}_0^{-T} \tilde{\mathbf{H}}^{\text{ref}} \mathbf{J}_0^{-1}$ is defined on element level. Again, a three-field functional of the form

$$\Pi_{\text{PH}}[\mathbf{d}, \boldsymbol{\alpha}, \mathbf{P}^*] = \int_{\Omega} (\overline{W}(\mathbf{H}^c + \tilde{\mathbf{H}}) - \underline{\mathbf{P}^*} : \tilde{\mathbf{H}}) \, dA \quad (36)$$

can be used as a variational basis. This time, orthogonality is required between the first Piola-Kirchhoff stress \mathbf{P}^* and the enhanced displacement gradient field $\tilde{\mathbf{H}}$ to remove the underlined term and reduce the formulation to a two-field principle. To compare this formulation with the one from Section 3.3.2 we compute the Green-Lagrange strain based on (33) as

$$\mathbf{E}(\mathbf{d}, \boldsymbol{\alpha}) = \mathbf{E}^c + \frac{1}{2} \left(\tilde{\mathbf{H}}^T + \tilde{\mathbf{H}} + \tilde{\mathbf{H}}^T \tilde{\mathbf{H}} + \mathbf{H}^{cT} \tilde{\mathbf{H}} + \mathbf{H}^c \tilde{\mathbf{H}}^T \right), \quad (37)$$

which is obviously more involved in terms of geometrical nonlinearity than the enhanced strain in Equation (29). One important consequence of this difference is the fact that also the geometric stiffness is affected by the enhanced part. The classical enhancement based on the *Wilson modes*⁴² is presented in Reference 12 as

$$\tilde{\mathbf{H}}^{\text{ref}} = \begin{bmatrix} \xi \alpha_1 & \eta \alpha_3 \\ \xi \alpha_4 & \eta \alpha_2 \end{bmatrix}. \quad (38)$$

The corresponding element will be denoted as Q1/H4 in the following.

An alternative enhancement of the displacement gradient are the “transposed Wilson modes” as proposed in Reference 21, given by

$$\mathbf{H}(\mathbf{d}, \boldsymbol{\alpha}) = \mathbf{H}^c(\mathbf{d}) + \mathbf{F}_0^c(\mathbf{d}) \tilde{\mathbf{H}}^T(\boldsymbol{\alpha}). \quad (39)$$

Here \mathbf{F}_0^c denotes the compatible deformation gradient evaluated at the element centroid. The specific construction is a prerequisite for frame-invariance of the element. The corresponding element is denoted as Q1/HT4.

3.3.4 | Further possible enhancements

Since a multitude of definitions of nonlinear strain measures is possible, each one is a potential candidate for an improved EAS formulation. Two contributions with a particular focus on hourglassing are mentioned in the following. Crisfield et al.⁴⁸ proposed an enhancement of the right stretch tensor and thus avoided geometric hourglassing for a large strain compression problem. There is, however, no specific discussion or explanation of the mechanism that avoids hourglassing. Within a Petrov-Galekin approach, Pfefferkorn & Betsch⁴⁹ proposed an interesting enhancement of the spatial deformation gradient. Numerical examples indicate that the element is free from geometric *and* material hourglassing. However, this comes at the cost of a more complex formulation as well as an unsymmetric stiffness matrix.

3.4 | Element analysis based on eigenvalues and eigenmodes

3.4.1 | Problem setup



Insight into element behavior can be gained by monitoring the eigenvalues of the hourglass modes of the element tangent stiffness matrices under homogeneous deformation states. We consider a rectangular element with aspect ratio $r_e = L_1^e/L_2^e$ under plane strain condition and a prescribed (homogeneous) stretch state $\mathbf{F} = \text{diag}(\lambda_1, \lambda_2)$. The hourglass eigenvalues are given as

$$\omega_i^{\text{hg}} = \boldsymbol{\Phi}_i^T \mathbf{k}_{\text{red}}(\lambda_1, \lambda_2) \boldsymbol{\Phi}_i \quad i = 1, 2, \quad (40)$$

with the reduced stiffness matrix defined in (28) and the normalized hourglass eigenvector $\boldsymbol{\Phi}_i$. A zero or negative hourglass eigenvalue is an indicator that geometric or material hourglassing is likely to occur. However, as shown in Reference 40, artificial instabilities can also be observed for small positive hourglass eigenvalues.

Extending the work of Armero¹⁶ we compute closed form expressions of the hourglass eigenvalues. The results are summarized in Table 3. The required coefficients of the tangents \mathbb{C} and \mathbb{A} (or \mathbf{C} and \mathbf{A} in matrix notation) are defined via the incremental stress-strain relations

TABLE 3 Hourglass eigenvalues

	ω_1^{hg} 	ω_2^{hg} 
Q1	$\frac{1}{3r_e} (A_{11}^n + r_e^2 A_{11}^s)$ $= \frac{\lambda_1^2 (C_{11}^n + r_e^2 C_{12}^s)}{3r_e} + \frac{(r_e^2 S_2 + S_1)}{3r_e}$	$\frac{1}{3r_e} (r_e^2 A_{22}^n + A_{22}^s)$ $= \frac{\lambda_2^2 (r_e^2 C_{22}^n + C_{12}^s)}{3r_e} + \frac{(r_e^2 S_2 + S_1)}{3r_e}$
Q1/E4	$\frac{\lambda_1^2 \det \mathbf{C}^n}{3r_e C_{22}^n} + \frac{(r_e^2 S_2 + S_1)}{3r_e}$	$\frac{r_e \lambda_2^2 \det \mathbf{C}^n}{3C_{11}^n} + \frac{(r_e^2 S_2 + S_1)}{3r_e}$
Q1/E2s	$\frac{\lambda_1^2 C_{11}^n}{3r_e} + \frac{(r_e^2 S_2 + S_1)}{3r_e}$	$\frac{r_e \lambda_2^2 C_{11}^n}{3} + \frac{(r_e^2 S_2 + S_1)}{3r_e}$
Q1/E2n	$\frac{\lambda_1^2 \det \mathbf{C}^n}{3r_e C_{22}^n} + \frac{r_e \lambda_1^2 C_{12}^s}{3} + \frac{(r_e^2 S_2 + S_1)}{3r_e}$	$\frac{r_e \lambda_2^2 \det \mathbf{C}^n}{3C_{11}^n} + \frac{\lambda_2^2 C_{12}^s}{3r_e} + \frac{(r_e^2 S_2 + S_1)}{3r_e}$
Q1/H4	$\frac{\det \mathbf{A}^n}{3r_e A_{11}^n} + \frac{r_e \det \mathbf{A}^s}{3A_{11}^s}$	$\frac{r_e \det \mathbf{A}^n}{3A_{11}^n} + \frac{\det \mathbf{A}^s}{3r_e A_{11}^s}$
Q1/HT4	$\frac{\det \mathbf{A}^n}{3r_e A_{22}^n}$	$\frac{r_e \det \mathbf{A}^n}{3A_{11}^n}$

$$\begin{bmatrix} \Delta P_{11} \\ \Delta P_{22} \\ \Delta P_{12} \\ \Delta P_{21} \end{bmatrix} = \mathbf{A} \Delta \mathbf{F} = \begin{bmatrix} A_{11}^n & A_{12}^n & 0 & 0 \\ A_{12}^n & A_{22}^n & 0 & 0 \\ 0 & 0 & A_{11}^s & A_{12}^s \\ 0 & 0 & A_{12}^s & A_{22}^s \end{bmatrix} \begin{bmatrix} \Delta F_{11} \\ \Delta F_{22} \\ \Delta F_{12} \\ \Delta F_{21} \end{bmatrix} \quad (41)$$

and

$$\begin{bmatrix} \Delta S_{11} \\ \Delta S_{22} \\ \Delta S_{12} \end{bmatrix} = \mathbf{C} \Delta \mathbf{E} = \begin{bmatrix} C_{11}^n & C_{12}^n & 0 \\ C_{12}^n & C_{22}^n & 0 \\ 0 & 0 & C_{12}^s \end{bmatrix} \begin{bmatrix} \Delta E_{11} \\ \Delta E_{22} \\ 2\Delta E_{12} \end{bmatrix}, \quad (42)$$

with sub-matrices \mathbf{A}^n , \mathbf{A}^s and \mathbf{C}^n defined by the respective blocks. Further details are given in Appendix B.

For the constitutive response we consider the so called special Blatz-Ko rubber,⁴¹ which is characterized by the remarkably simple strain-energy function

$$\overline{W}(\lambda_1, \lambda_2) = \frac{\mu}{2} \left(\frac{1}{\lambda_1^2} + \frac{1}{\lambda_2^2} + 2\lambda_1 \lambda_2 - 4 \right), \quad (43)$$

with the shear modulus μ as only material parameter. Besides its simplicity, the main motif to use this model is its strain softening response under tension, relevant for the analysis of material hourglassing. For the plane strain case it was shown by Knowles and Sternberg⁵¹ (see also Horgan⁵²) that material stability, that is, ellipticity of the underlying equilibrium equations, is bounded by

$$2 - \sqrt{3} < \frac{\lambda_1}{\lambda_2} < 2 + \sqrt{3}. \quad (44)$$

Figure 3A shows the boundary of ellipticity condition (42), the relation between the stretches for a uniaxial and biaxial stress state as well as the contour lines where the determinant of the sub-matrices vanishes, that is, the respective tangent loses its positive definiteness. For the case of uniaxial tension in X_2 -direction ($S_{11} = 0$, $S_{22} \neq 0$) these lines indicate the onset of strain softening in the respective stress strain relation, see Figure 3B. Here, strain softening occurs slightly before ellipticity is lost. This becomes particularly interesting in Section 5.4 where physical instabilities as well as material hourglassing occurs.

3.4.2 | Example I: Uniaxial stress state

First, we consider a homogeneous uniaxial stress state governed by the principal stress

$$S_1 = 0 \Rightarrow \lambda_1 = 3\lambda_2^{-1/3}, \quad S_2 = \frac{1}{\lambda_2} W_{,\lambda_2} = \mu \frac{(\lambda_2^{8/3} - 1)}{\lambda_2^4}. \quad (45)$$

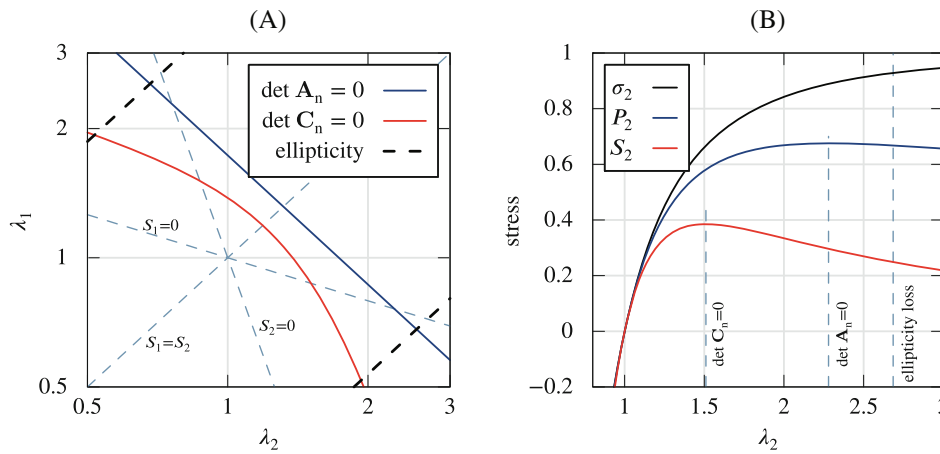


FIGURE 3 (A) Isolines of various quantities in the λ_1 - λ_2 -plane. The thick dashed lines indicate the boundaries where ellipticity is lost, see Equation (42); (B) various stress quantities for a uniaxial stress state with $S_1 = 0$

Thus, all following quantities can be expressed as a function of λ_2 . In particular, Figure 4 shows both hourglass eigenvalues for the elements described in Sections 3.3.2 and 3.3.3 as functions of λ_2 . Also the newly proposed elements Q1/ME4, Q1/MH4-I and Q1/MH4-II (discussed in Section 4) are included. Due to the compressible material as well as $r_e = 1$, locking is not very pronounced in this case and the eigenvalues for the undeformed case $\lambda_2 = 1$ are only slightly larger for Q1 than for the EAS elements.

For compressive deformations, $\lambda_2 < 1$, both standard EAS formulations Q1/E4 and Q1/H4 suffer from geometric hourglassing, which is reflected by the zero eigenvalue $\omega_1^{hg} = 0$ at $\lambda_2 \approx 0.73$ (cf. Figure 4A,C). This defect is obviously not present for Q1/E2n. The element is “stabilized” by shear locking. Also Q1/HT4 as well as the newly proposed Q1/ME4 are stable in this case due to the implicit elimination of the geometric stiffness for the hourglass modes. For Q1/H4 the destabilizing geometric terms arise from the shear contributions. Their extrapolation around the reference state provide

$$\frac{r_e \det \mathbf{A}^s}{3A_{22}^s} \approx \frac{r_e}{3} \Delta S_2 \quad \text{and} \quad \frac{\det \mathbf{A}^s}{3r_e A_{11}^s} \approx \frac{1}{3r_e} \Delta S_2, \tag{46}$$

for ω_1^{hg} and ω_2^{hg} , respectively (cf. Table 3). For $\Delta S_2 = \gamma_c p$, these expressions formally resemble the critical geometric terms in estimates (9) and (10). However, due to the moderate aspect ratio, as well as an increase in axial stiffness C_{22}^n (due to compression in X_2 -direction), a softening of ω_2 is not observed for this example.

For the case of tensile deformation, $\lambda_2 > 1$, some eigenvalues pass through zero, which is an indication for material hourglassing. Let us first focus on Figure 4A. The Q1/E4 element has a zero eigenvalue ω_1^{hg} right after a horizontal tangent occurs in the S_2 - λ_2 -relation (Figure 3B) at $\lambda_2 = 3^{3/8} \approx 1.51$. With further stretching, ω_1^{hg} tends quickly to minus infinity when the axial stiffness becomes $C_{22}^n = 0$ at $\lambda_2 = 2^{3/4} \approx 1.68$. The cause for that can be illustrated by the limit value of the first hourglass eigenvalue of Q1/E4:

$$\lim_{C_{22}^n \rightarrow +0} \left(\frac{\lambda_1^2 C_{11}^n}{3r_e} - \frac{\lambda_1^2 (C_{12}^n)^2}{3r_e C_{22}^n} + \frac{r_e^2 S_2}{3r_e} \right) = -\infty \quad \text{with } C_{11}^n, C_{12}^n > 0. \tag{47}$$

Here, the underlined part corresponds to the volumetric EAS terms which, on the one hand eliminates volumetric locking (reflected by $C_{11}^n \rightarrow \infty$ in the incompressible limit) and on the other hand, is responsible for triggering material hourglassing due to the large negative stiffness when C_{22}^n approaches zero (e.g., due to strain softening). Similar considerations explain why the second hourglass eigenvalue ω_2^{hg} becomes negative.

The results for Q1/H4 and Q1/HT4 are depicted in Figure 4C and they qualitatively confirm the results reported in Reference 16. For these elements, a zero eigenvalue ω_1^{hg} is related to an horizontal tangent in the P_2 - λ_2 -relation at $\lambda_2 = 3^{3/4}$. However, no singularity is obtained, since A_{22}^n , in contrast to C_{22}^n , does not approach zero but remains positive due to the

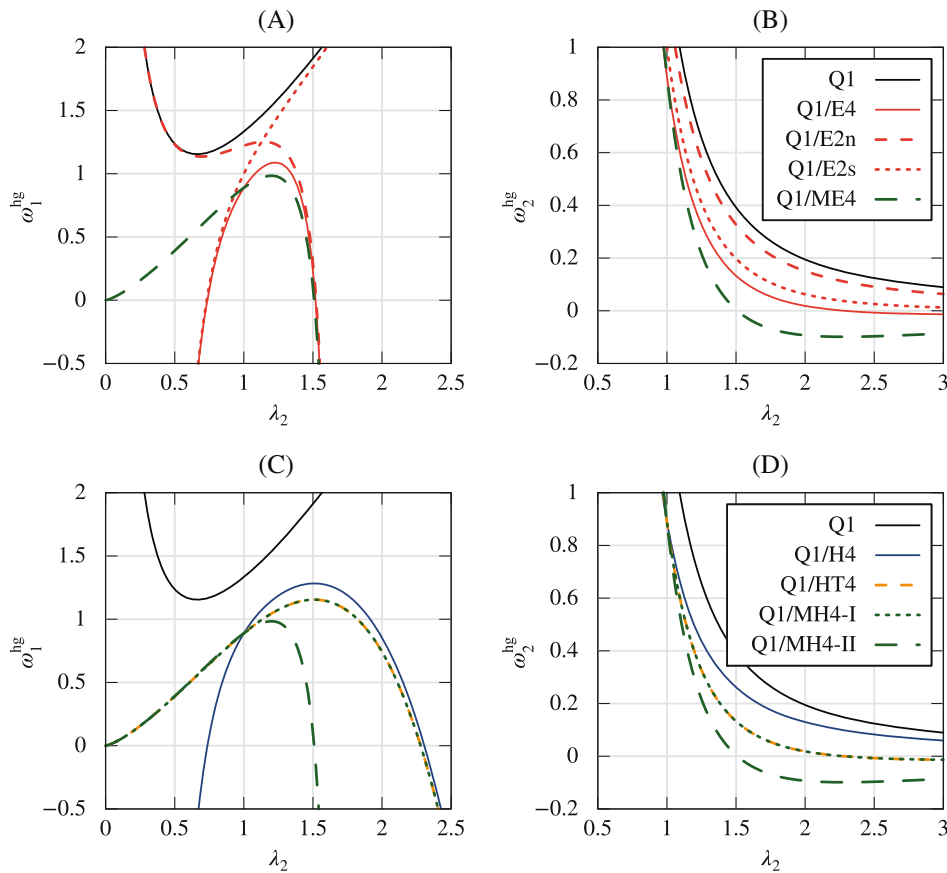


FIGURE 4 Uniaxial stress state ($S_1 = 0$), $r_e = 1$, both hourglass eigenvalues as a function of λ_2

geometric terms involved. For Q1/HT4 the zero eigenvalue arises slightly earlier than for Q1/H4 due to the absence of the geometric hourglass stiffness. The situation is different for ω_2^{hg} . It becomes negative for Q1/HT4, while it remains positive for Q1/H4. This can be explained by the stabilizing effect of the EAS induced geometric stiffness, present only for the Q1/H4 (cf. Equation (44)₂).

3.4.3 | Example II: Biaxial stress state

Next, we consider a biaxial stress state

$$S_1 = \mu \frac{\lambda_1^3 \lambda_2 - 1}{\lambda_1^4}, \quad S_2 = \mu \frac{\lambda_2^3 \lambda_1 - 1}{\lambda_2^4}, \quad (48)$$

with *independently* prescribed stretches λ_1 and λ_2 . The objective is to cover a broader range of (still homogeneous) strain states.

Figure 5A,B visualize the roots of various eigenvalues ω_i^{hg} . The filled regions, enveloped by the corresponding root, represent domains with negative eigenvalues, whereas everywhere else the corresponding eigenvalue is positive. Uniaxial stress states are represented by dashed lines and its intersections with the lines of zero eigenvalues coincide with the zero eigenvalues in Figure 4.

Geometric hourglassing does not occur for Q1/ME4, Q1/MH4-I and Q1/HT4 and, similar to the uniaxial case in Example I, no negative eigenvalue occurs for the compression case ($S_2 \leq 0$ and $S_1 \leq 0$). For Q1/H4 and Q1/E4; however, ω_1^{hg} becomes zero in the compressive domain. Interestingly, the root of Q1/H4 falls below the one of Q1/E4, indicating that the corresponding eigenvalue of Q1/H4, and thus the hourglass stiffness, is smaller. The reason for this phenomenon is the contribution of the EAS terms to the (negative) geometric stiffness. Material hourglassing shows up for all considered

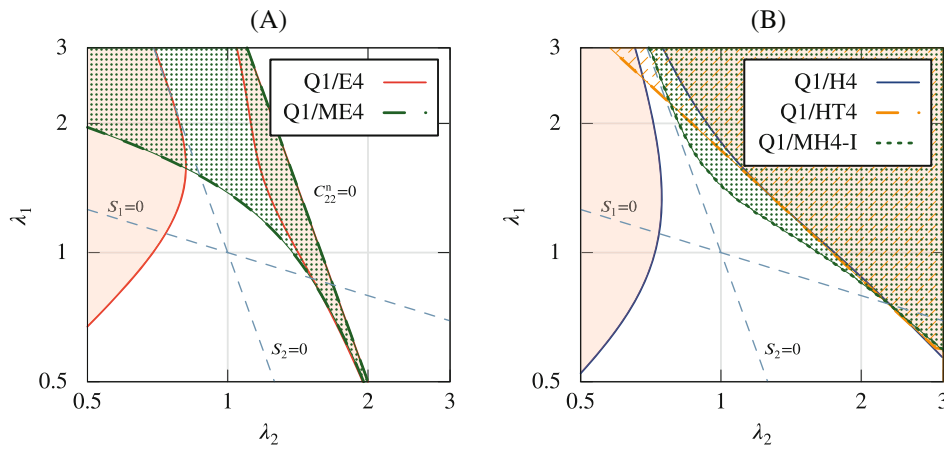


FIGURE 5 Biaxial stress state, $r_e = 1$, the colored lines indicate a zero eigenvalue $\omega_1^{\text{hg}}(\lambda_1, \lambda_2) = 0$. They envelope the filled regions, in which the corresponding eigenvalue is negative

EAS elements. The branches of Q1/ME4 and Q1/HT4 in Figure 5A,B are identical to the ones of $\det \mathbf{C}_n = 0$ and $\det \mathbf{A}_n = 0$, respectively, in Figure 3A. Furthermore, Figure 5A shows that both “E”-enhanced elements share the same envelope, which also corresponds to $C_{22}^n = 0$. Here, the eigenvalue becomes infinite, compare Equation (45), and subsequently a further sign change occurs.

4 | STABILIZATION CONCEPT TO AVOID GEOMETRIC HOURGLASSING

4.1 | Principal idea

Let us consider an additive split of a generic (possibly enhanced) displacement gradient $\mathbf{H} = \mathbf{H}_r + \mathbf{H}_h$, where \mathbf{H}_h denotes the part that is responsible for hourglassing and has yet to be identified and \mathbf{H}_r the remaining part. With this definition, the geometric part of the element stiffness matrix reads

$$\mathbf{k}_g = \int_{\Omega} \frac{1}{2} \left(\mathbf{H}_r^T \mathbf{H}_r + \mathbf{H}_r^T \mathbf{H}_h + \mathbf{H}_h^T \mathbf{H}_r + \underline{\mathbf{H}_h^T \mathbf{H}_h} \right)_{,\dot{\mathbf{d}}} : \mathbf{S} \, dA, \quad (49)$$

where $\dot{\mathbf{d}}$ represents a generic element vector of degrees of freedom (e.g., $\dot{\mathbf{d}} = [\mathbf{d} \quad \boldsymbol{\alpha}]^T$). The underlined term is the one which can trigger geometric hourglassing. An obvious option to avoid geometric hourglassing is to remove this term from the definition of the geometric tangent, as proposed by Reese et al.⁸ in the context of a reduced integration concept with physical stabilization. This, however, requires the stabilization procedure to be constant, at least within each increment, to preserve quadratic convergence in the nonlinear solution process.

The stabilization concept proposed herein is more general (see the various element formulations below), quadratic convergence is automatically preserved and, most importantly, only minor changes in existing element routines are required. The idea is to drop precisely this destabilizing part $\mathbf{H}_h^T \mathbf{H}_h$ in the definition of a modified (discrete) Green-Lagrange strain

$$\dot{\mathbf{E}} := \mathbf{E}_{\text{lin}} + \frac{1}{2} \left(\mathbf{H}_r^T \mathbf{H}_r + \mathbf{H}_r^T \mathbf{H}_h + \mathbf{H}_h^T \mathbf{H}_r \right) \quad (50)$$

with $\mathbf{E}_{\text{lin}} = \text{sym}(\mathbf{H})$ being the unmodified (possibly enhanced) geometrically linear part of the strain tensor. The definition of \mathbf{H}_h depends on the finite element formulation and may be obtained by an investigation of the element stiffness matrix. Since hourglassing is related to higher order terms only, the modification does not affect the constant strain modes, which are always included in \mathbf{H}_r and thus consistency of the finite element formulation is not affected. This also guarantees convergence towards physically correct instabilities with mesh refinement.

The technical implications on the framework of a finite element procedure are fairly simple. For consistent linearization, the definition in Equation (50) requires the modified operators

$$\delta \dot{\mathbf{E}} = \dot{\mathbf{B}} \delta \dot{\mathbf{d}} \quad \text{and} \quad \Delta \delta \dot{\mathbf{E}} : \mathbf{S} = \delta \dot{\mathbf{d}}^T \dot{\mathbf{G}}(\dot{\mathbf{E}}, \mathbf{S}) \Delta \dot{\mathbf{d}} \quad (51)$$

for computation of the residual vector as well as the material and geometric stiffness matrix. In this process, the stress and elastic tangent are computed as a function of the modified strain measure, that is, $\mathbf{S}(\dot{\mathbf{E}})$ and $\mathbf{C}(\dot{\mathbf{E}})$. Further implementation aspects are discussed in Appendix C.

4.2 | Examples

4.2.1 | Stabilized element Q1/ME4

As shown in the preceding sections, geometric hourglassing of the Q1/E4 element is triggered by the geometric stiffness coming from the *compatible* bilinear hourglass modes. Employing a split of the compatible part of the displacement gradient into a constant and linear part

$$\mathbf{H}^c(\xi, \eta) = \mathbf{H}_0^c + \mathbf{H}_1^c(\xi, \eta) \quad \text{with} \quad \mathbf{H}_0^c = \mathbf{H}^c \Big|_{\xi=\eta=0}, \quad (52)$$

we can define

$$\mathbf{H}_r := \mathbf{H}_0^c \quad \text{and} \quad \mathbf{H}_h := \mathbf{H}_1^c \quad (53)$$

and obtain a modified expression for the compatible part of the Green-Lagrange strain in (29) as

$$\dot{\mathbf{E}}^c = \frac{1}{2} \left[\underbrace{\mathbf{H}_0^c + \mathbf{H}_0^{cT} + \mathbf{H}_1^c + \mathbf{H}_1^{cT}}_{2\dot{\mathbf{E}}_{\text{lin}}^c} + \underbrace{\mathbf{H}_0^{cT} \mathbf{H}_0^c + \mathbf{H}_0^{cT} \mathbf{H}_1^c + \mathbf{H}_1^{cT} \mathbf{H}_0^c}_{2\dot{\mathbf{E}}_{\text{quad}}^c} \right]. \quad (54)$$

Within the EAS framework, the modified strain (29) is adapted as $\mathbf{E} = \dot{\mathbf{E}}^c + \tilde{\mathbf{E}}$ and the resulting element is denoted as Q1/ME4. In view of the modal analysis of Section 3.4, the corresponding hourglass eigenvalues reduce to $\omega_1^{\text{hg}} = \frac{\lambda_1^2 \det \mathbf{C}^n}{3r_e C_{22}^n}$ and $\omega_2^{\text{hg}} = \frac{\lambda_2^2 r_e \det \mathbf{C}^n}{3C_{11}^n}$. These are identical to the ones of Q1/E4 without geometric terms in Table 3. Figures 4 and 5 show that, similar to Q1/HT4, the element's eigenvalues remain positive under compression.

4.2.2 | Stabilized element Q2/ME11

Like its bilinear counterpart, the biquadric element Q2/E11 suffers from geometric hourglassing, which is triggered by the geometric stiffness of certain compatible displacement modes. However, the order of locking is shifted to quadratic displacement modes.[#] Similar as before, we consider a Taylor expansion of the compatible displacement gradient of the form

$$\mathbf{H}^c = \mathbf{H}_0^c + \mathbf{H}_1^c(\xi, \eta) + \mathbf{H}_2^c(\xi^2, \eta^2, \xi\eta) + \mathbf{H}_3^c(\xi^2\eta, \xi\eta^2, \xi^2\eta^2). \quad (55)$$

For the uniaxial compression test, numerical investigations indicate that the last two terms trigger “higher order” geometric hourglassing. Thus we define

$$\mathbf{H}_r := \mathbf{H}_0^c + \mathbf{H}_1^c \quad \text{and} \quad \mathbf{H}_h := \mathbf{H}_2^c + \mathbf{H}_3^c \quad (56)$$

and proceed as before. As not necessarily *all* geometric stiffness contributions from (53)₂ are responsible for geometric hourglassing, alternative definitions of \mathbf{H}_h are possible. The corresponding element is denoted as Q2/ME11.

4.2.3 | Stabilized element Q1/MH4-I and Q1/MH4-II

Also Q1/H4 suffers from geometric hourglassing and the remedy described in Section 4.2.1 can also be applied to this element formulation. The element is denoted as Q1/MH4-I with $\mathbf{H}_r = \mathbf{H}_0^c + \tilde{\mathbf{H}}$ and $\mathbf{H}_h = \mathbf{H}_1^c$. The eigenvalue is then modified according to

$$\omega_1^{\text{hg}} = \frac{\det \mathbf{A}^n}{3r_e A_{22}^n} + C_{12}^s \left(\frac{r_e \lambda_1^2}{3} + \frac{\lambda_2^2}{3r_e} \right) - \frac{A_{22}^s}{3r_e} - \frac{r_e (A_{12}^s)^2}{3A_{22}^s} \quad (55)$$

$$\omega_2^{\text{hg}} = \frac{r_e \det \mathbf{A}^n}{3A_{11}^n} + C_{12}^s \left(\frac{r_e \lambda_1^2}{3} + \frac{\lambda_2^2}{3r_e} \right) - \frac{r_e A_{11}^s}{3} - \frac{(A_{12}^s)^2}{3r_e A_{11}^s} \quad (56)$$

However, in contrast to Q1/E4, the shear strain enhancement of Q1/H4 contains also a quadratic part $\tilde{\mathbf{H}}^T \tilde{\mathbf{H}}$, which causes an additional geometric hourglassing phenomenon, see Section 2. In order to avoid it, we redefine the strain enhancement of Q1/H4 from Equation (35) as

$$\dot{\mathbf{E}} = \dot{\mathbf{E}}^c + \frac{1}{2} \left(\tilde{\mathbf{H}}^T + \tilde{\mathbf{H}} + \mathbf{H}^{c^T} \tilde{\mathbf{H}} + \mathbf{H}^c \tilde{\mathbf{H}}^T \right). \quad (59)$$

The element is denoted as Q1/MH4-II. For undistorted elements and homogeneous strain states, where the mixed terms are not activated, it provides the same results as Q1/ME4.

4.2.4 | Stabilization of assumed stress element Q1/S5

The proposed stabilization procedure can also be applied to the assumed stress elements by Pian and Sumihara.⁵³ Within this work we consider a total Lagrangian formulation based on an independent second Piola-Kirchhoff stress field. The required inverse stress-strain relation of the Neo-Hookean material is adopted from Reference 54. We refer to the work of Viebahn et al.¹⁷ for further details. The stabilized version, denoted as Q1/MS5, is based on the modified Green-Lagrange strain (54).

4.3 | Discussion

By design, the proposed stabilization concept modifies element stiffness such that geometric hourglassing, occurring under compressive states of stress, is effectively removed. The same modifications; however, apparently have a detrimental, destabilizing effect in the context of material hourglassing for states of tensile stress. However, as material hourglassing emanates from artefacts in the material stiffness, not from the geometric stiffness, this is not an issue in the authors' opinion. Stabilizing the elements in the tensile regime by adding (not removing, respectively) artificial geometric stiffness would substantiate a strategy of balancing one error with another one. For material hourglassing (as for any parasitic or unphysical behavior) removing the source of the problem instead of fighting its symptoms is the way to go. Moreover, a broad class of problems do not involve material hourglassing anyway.

The nature of material hourglassing is quite different from the one of geometric hourglassing. The modal analysis in Section 3.4 and the benchmark in Section 5.4 imply that whether or not geometric terms are involved might be of little relevance.

The proposed methodology can be viewed as a self-adaptive stabilization approach in the sense that the element's linear response is not affected and only the onset of geometric nonlinearity will activate the strain modification.

Here, the definition of \mathbf{H}_h is based on a stability analysis of an *undistorted* element and we do not claim that hourglassing is fully avoided for distorted mesh configurations. Numerical experiments, however, indicate an hourglassing-free performance also for severely distorted meshes.

Throughout this work, the concept of "stiffness" is used to analyze the elements. Nevertheless, for explicit computations, which are solely based on residual quantities, this approach is straightforwardly applicable via the modified operator (48)₁.

A further aspect is the fact that the proposed modification of the strain tensor (50) implies that $\det \hat{\mathbf{C}} < 0$ (self-penetration of matter) is possible, with $\hat{\mathbf{C}} = 2\hat{\mathbf{E}} - \mathbf{1}$ being the modified right Cauchy-Green tensor. Exemplified for a pure bending deformation $u_1 = c_5 \xi \eta$ of a square Q1/ME4 element, it can be shown that at location $\eta = \eta_0$ (e.g., an integration point), $\det \hat{\mathbf{C}}$ becomes zero for $c_5 = 1/(2\eta_0)$. As this corresponds to very large in-plane bending deformations it is of minor relevance for practical computations. More importantly, with mesh refinement this defect vanishes. However, possible remedies can be found by adding volumetric stabilization terms, see Reference 21.

5 | PHYSICAL VERSUS ARTIFICIAL INSTABILITIES: SOME ANALYTICAL AND NUMERICAL RESULTS

5.1 | Motivation

Availability of mathematical tools to analyze finite element solutions of nonlinear problems is limited, which underlines the importance of numerical benchmarks. Design of feasible benchmarks is not trivial, since a unique solution does not always exist and critical points, such as limit points or bifurcation points can occur and exhaustive analytical solutions are rarely available.

In this section we propose a simple bifurcation problem, for which analytical solutions can be obtained, as a benchmark tailored to study stability properties of finite elements in large strain nonlinear analysis. The comparison with numerical results provides insight on the stability properties of the elements discussed in the preceding sections.

5.2 | Problem setup: Bifurcation of a hyperelastic rectangular block

Let us consider a rectangular block with dimensions $2L_1 \times 2L_2$, made of an isotropic, compressible, hyperelastic material. The reference configuration \mathcal{B} is assumed to be stress-free and plane strain conditions apply, that is, $\lambda_3 = 1$. The block is constrained at $X_2 = \pm L_2$ by a prescribed vertical displacement $u_2(X_1, \pm L_2) = \pm \gamma \hat{u}_2$ with zero shear tractions (roller support), whereas the lateral edges at $X_1 = \pm L_1$ remain completely traction-free, see Figure 6. Horizontal rigid body modes are assumed to be restricted. With these boundary conditions at hand, the solution of the displacement-controlled problem is governed by the weak equilibrium equation

$$\Pi_{,\mathbf{u}}[\mathbf{u}, \gamma] \delta \mathbf{u} = \int_B \delta \mathbf{F} : \mathbf{P}(\mathbf{u}, \gamma) \, dA = 0, \quad (60)$$

with admissible virtual displacement $\delta \mathbf{u}$. For a sufficiently small load factor γ a unique solution (the minimizer of Π) is given by the deformed configuration $2L_1 \lambda_1 \times 2L_2 \lambda_2$, with a homogeneous uniaxial stress state and biaxial stretching

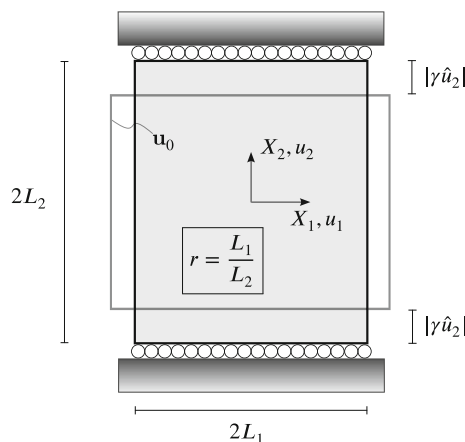


FIGURE 6 Problem description exemplified for a compression test

$$\mathbf{P} = \text{diag}(0, P_2) \quad \text{and} \quad \mathbf{F} = \text{diag}(\lambda_1(\lambda_2), \lambda_2), \quad \text{with} \quad \lambda_2(\gamma) = 1 + \gamma \hat{u}_2/L_2. \quad (61)$$

The corresponding displacement field $\mathbf{u}_0(\mathbf{X}, \gamma)$ marks the primary path of the solution. In the subsequent analysis we focus on critical points on the primary path at which bifurcation into secondary equilibrium paths may be triggered. They are associated with critical stretches $\lambda_2 =: \lambda_c^{(j)}$. Here, integer j denotes the j^{th} bifurcation point and $\Delta \mathbf{u}^{(j)}$ is the corresponding incremental bifurcation mode (buckling mode). The criterion for a critical point is given by the *incremental* eigenvalue problem

$$(\Pi_{,\mathbf{u}} \delta \mathbf{u})_{,\mathbf{u}} \Delta \mathbf{u}^{(j)} = \int_B \delta \mathbf{F} : \underbrace{\mathbb{A}(\mathbf{u}_0, \lambda_c^{(j)})}_{\Delta \mathbf{P}^{(j)}} : \text{Grad} \Delta \mathbf{u}^{(j)} \, dA = 0, \quad (62)$$

subjected to the incremental boundary conditions

$$\Delta P_{11}^{(j)}(\pm L_1, X_2) = 0, \quad \Delta P_{12}^{(j)}(\pm L_1, X_2) = 0, \quad \Delta P_{21}^{(j)}(X_1, \pm L_2) = 0, \quad \Delta u^{(j)}(X_1, \pm L_2) = 0. \quad (63)$$

This bifurcation problem is well studied in the literature, including *analytical solutions* for criterion (59), and we refer to Appendix D for further details and references. The exact location of the bifurcation point in the *numerical solution* of (59) along with the corresponding bifurcation mode can be found with the method of extended systems as a direct approach, see Reference 55 and, in the context of displacement-controlled loading.⁵⁶

5.3 | Geometric instabilities–Compression test

5.3.1 | Setup and reference solution

We first consider a block with Neo-Hookean material under compression, such that $\hat{u}_2 < 0$, $P_2 < 0$ and $\lambda_2 < 1$. The corresponding strain energy function is given by

$$\overline{W}(\lambda_1, \lambda_2) = \frac{\mu}{2}(\lambda_1^{-2} + \lambda_2^{-2} - 2) - \mu \ln(\lambda_1 \lambda_2) + \frac{\Lambda}{2} \ln(\lambda_1 \lambda_2)^2. \quad (64)$$

Similar to Equation (43), the stress-free condition $S_1 = 0$ allows to eliminate one stretch component

$$S_1 = \frac{\mu \lambda_1^2 + \Lambda \ln(\lambda_1 \lambda_2) - \mu}{\lambda_1^2} = 0 \quad \Rightarrow \quad \lambda_1 = \exp \left(\frac{\mu}{\Lambda} - \frac{W_L \left(\frac{2\mu \exp(2\mu/\Lambda)}{\Lambda \lambda_2^2} \right)}{2} \right) \frac{1}{\lambda_2}. \quad (65)$$

Here, W_L is the Lambert W function. Next, we study the stability properties of the block in dependence of its aspect ratio $r = L_1/L_2$ in the undeformed configuration. The stability spectrum in Figure 7 shows the first four critical stretches $\lambda_c^{(j)}$ that appear along the primary path as a function of r . As expected, high sensitivity with respect to the aspect ratio r is observed. Tall, skinny blocks $r \rightarrow 0$ buckle in accordance with Euler's solution for buckling of beams, whereas for the "thick" limit $r \rightarrow \infty$ all critical branches converge towards the same value, which physically characterises surface buckling of an infinite half-space.

These results are the basis for the subsequent assessment of the various finite element formulations w.r.t. geometric hourglassing. As well known from linear problems, displacement based finite element formulations perform too stiff, that is, for a loading by prescribed external forces, displacements are underestimated and converge towards the correct solution from below (cf. "best approximation property",⁵⁷ Chap. 4.1). Although not generally supported by mathematical proofs, the same phenomenon is observed in nonlinear problems. For the present case of prescribed displacements this means that the resulting reaction forces converge from above. This implies that critical loads are *overestimated*. From this assertion, the following can be derived:

- An approximation of the j^{th} branch should not appear above the analytical solution of that branch (note that the vertical axis depicts the stretch in vertical direction, not the load factor).

- Consequently, none of the displacement based finite element approximations of a bifurcation branch in Figure 7 should appear in the stable region above the analytic curves.

As shown in References 58,59, the convergence properties of EAS elements are similar for linear problems, that is, displacements converge from below for load cases with prescribed forces and reaction forces converge from above for load cases with prescribed displacements. In the nonlinear regime, however, we observe violations of (i) and (ii), associated with an hourglass instability. Therefore, in the subsequent analysis we use conditions (i) and (ii) as criteria to detect hourglassing without visual inspection of the corresponding buckling modes.

Remark 1. This work focuses only on the incremental bifurcation problem itself and post-bifurcation states (e.g., triggered via perturbation methods) are not further considered. Here, the block’s aspect ratio plays a crucial role. As known from structural models, small aspect ratios yield stable bifurcated equilibrium branches whereas thicker blocks exhibit unstable ones (generating a limit point). For the present example, this change occurs at $r \approx 0.7$. For a corresponding theoretical analysis the interested reader is referred to Triantafyllidis et al.⁶⁰

5.3.2 | Influence of the aspect ratio

For the first test we consider a mesh with the same number of elements in both directions and only vary the block’s aspect ratio, such that always $r = r_e$, with r_e being the aspect ratio of an individual finite element. As a consequence, highly distorted elements are obtained in the limit cases. For $r \rightarrow 0$ we recover the thin beam limit, which would require only one single layer of (locking-free) elements across the thickness (X_1 -direction) and a number of elements in X_2 -direction to resolve the Euler buckling modes, that is, a $1 \times n$ -mesh would be optimal in terms of computational efficiency. Interestingly, the naive idea of using an $n \times 1$ -mesh instead for the opposite limiting case $r \rightarrow \infty$ is not feasible, because a single element along the lateral boundaries $X_1 = \pm L_1$ is unable to properly resolve the surface buckling modes. In this case, depending on the number of modes to be resolved, a locally refined mesh at the boundary would be “optimal”. This, however, is only a sideremark, because this benchmark is tailored to detect hourglass instabilities of specific finite element formulations and not to assess their efficiency (coarse mesh accuracy) in solving the problem at hand.

The graphs in Figure 8 show the critical stretches computed with Q1 and Q2 elements as well as various EAS formulations. The results obtained with a mesh with 8×8 elements are compared with the ones of a single element (dashed)

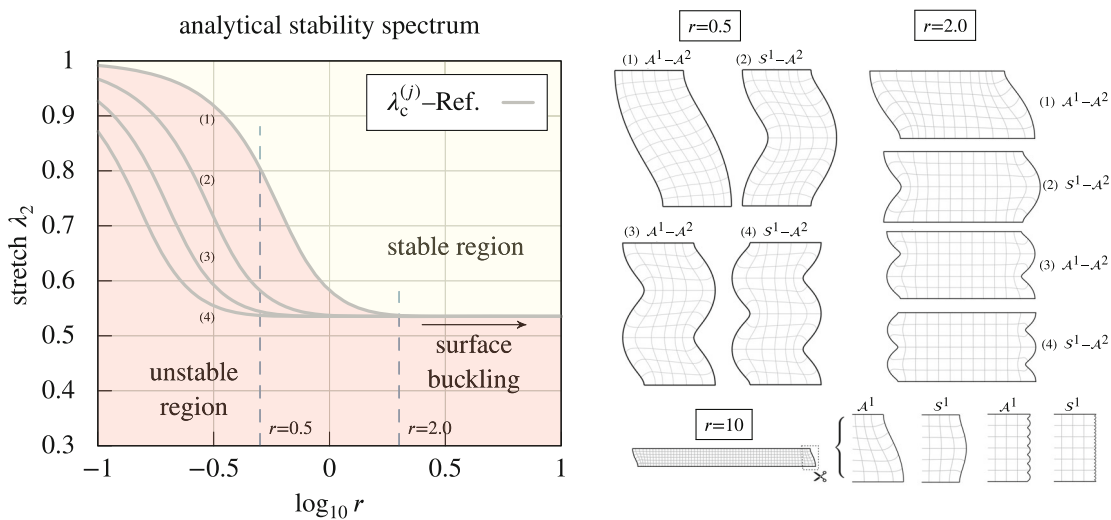


FIGURE 7 Left: geometric stability spectrum with analytical solution of the first four bifurcation points, Neo-Hooke with $E = 1000$, $\nu = 0.45$ ($\Lambda \approx 3103.448$, $\mu \approx 344.827$), corresponding numerical data are provided in Table D1 in Appendix D; right: contour plot of various buckling modes, superimposed on the undeformed geometry, exemplified for three aspect ratios. Here, the detailed surface buckling patterns for $r = 10$ are exemplified for mode numbers $n = \{1, 1, 8, 20\}$ (from left to right) and S^i/A^i designate symmetric/antisymmetric modes w.r.t the X_i -axis

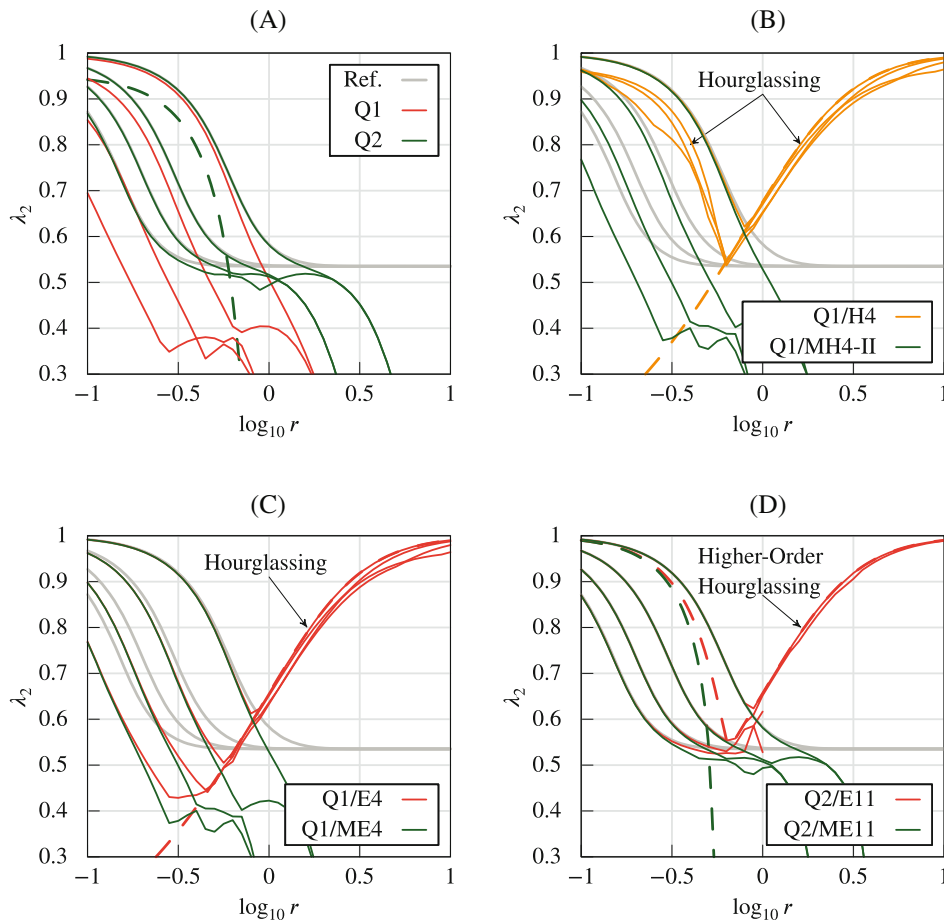


FIGURE 8 Geometric stability spectrum, analytical solution versus various FE formulations, mesh: 8×8 and 1×1 (dashed), Neo-Hooke $E = 1000$, $\nu = 0.45$. Due to numerical difficulties, some higher-order hourglassing-related branches are not fully displayed

as well as the analytical solution (thick grey). As expected, the results of the displacement based elements (A) fulfill condition (i) and (ii), whereas all standard EAS formulations (B)–(D) surpass some critical reference branches for certain aspect ratios.

For large r_e artificial instabilities occur for both meshes which is the “classical hourglassing”, driven by the geometric stiffness of higher-order compatible strain modes. On the other hand, small values of r_e only cause problems for Q1/H4 and Q1/H4-I (not shown), which is the “Euler buckling” on element level, driven by the geometric contributions of the enhanced strain part (cf. curvature-related P - Δ -effect in Figure 1D).

Since the boundary conditions hinder a constraint-free development of this hourglass pattern this effect is less pronounced for this example than the former hourglass effect. Typical examples of both hourglass patterns are sketched in Figure 9B.

In contrast to this, the modified element formulation Q1/ME4 (for this problem equivalent to Q1/MH4-II), as well as Q1/HT4 (not shown), fully avoid both hourglass effects and, importantly, no loss of accuracy is observed in regions where also the standard elements perform well. Some buckling modes are exemplarily sketched in Figure 9A.

Remark 2. Bifurcation points are characterized by a zero-crossing eigenvalue of the stiffness matrix. This information can then be used as a criterion to start a more accurate computation of the critical points via extended systems. For this problem, one usually observes that physical instabilities are reflected by a smooth propagation of the critical eigenvalues, whereas the onset of hourglass instabilities appear abruptly. From a numerical point of view this often causes difficulties in the computation of (artificial) critical points via extended systems and bisection algorithms may alternatively be used.

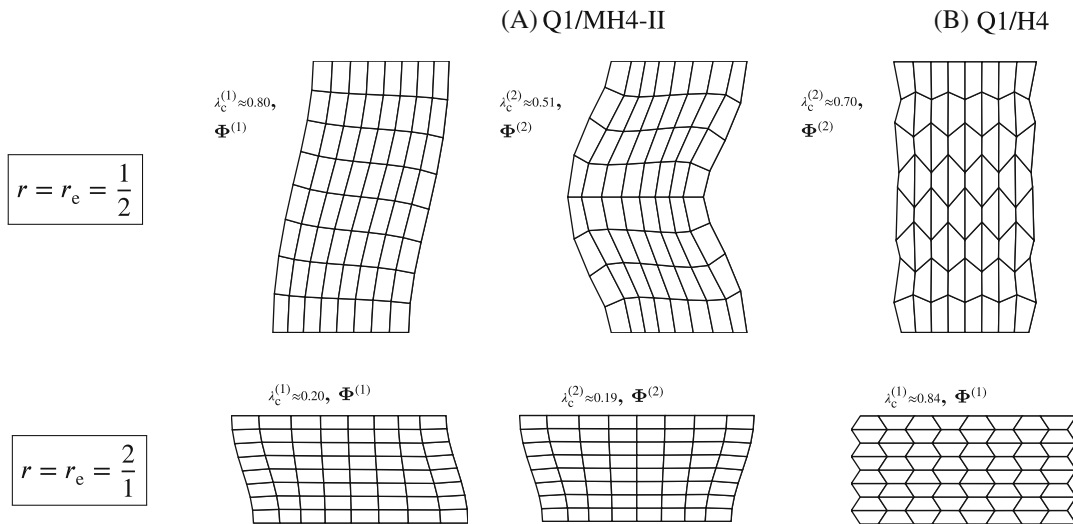


FIGURE 9 Geometric instabilities; buckling modes superimposed on the undeformed mesh configuration

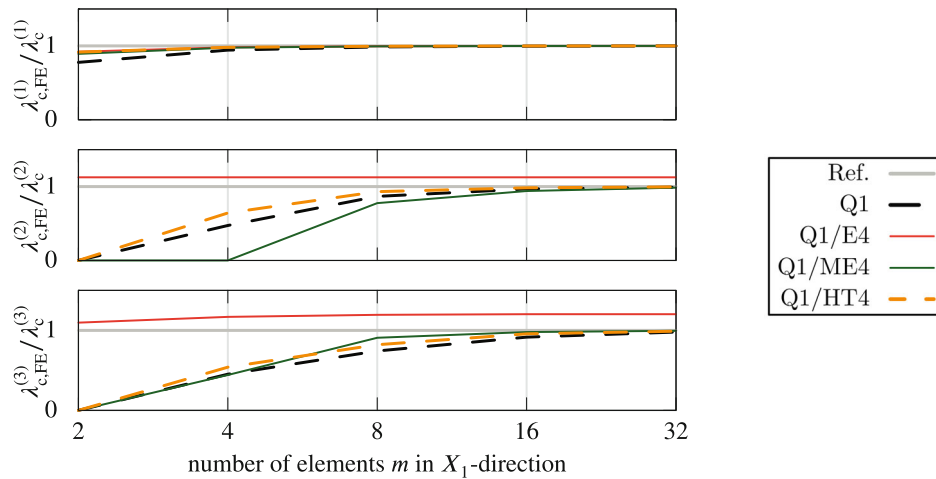


FIGURE 10 Convergence behavior towards the first 3 critical points, mesh: $m \times 2m$, Neo-Hooke $E = 1000$, $\nu = 0.45$

5.3.3 | Convergence study

For the second test we consider a tall block with $r = 1/2$ and a uniform $m \times 2m$ mesh such that the element's aspect ratio is $r_e = 1$. Figure 10 shows the normalized value $\lambda_{c,FE}^{(j)} / \lambda_c^{(j)}$ for the first three critical points versus m .

Q1 and Q1/ME4 are able to capture the critical points properly with mesh refinement without showing any sign of hourglassing. The small difference between both is due to mild locking of Q1. For $j = 1$, the Q1/E4 shows a slightly better convergence than the Q1/ME4 which can be explained by the absence of the geometric hourglass stiffness. However, the higher critical points $j = 2, 3$ are overestimated due to hourglassing. Similar results (not shown) are obtained for the Q1/H4 (cf. Q1/E4) and the Q1/MH4-I (cf. Q1/HT4), see also the numerical values in Table 4.

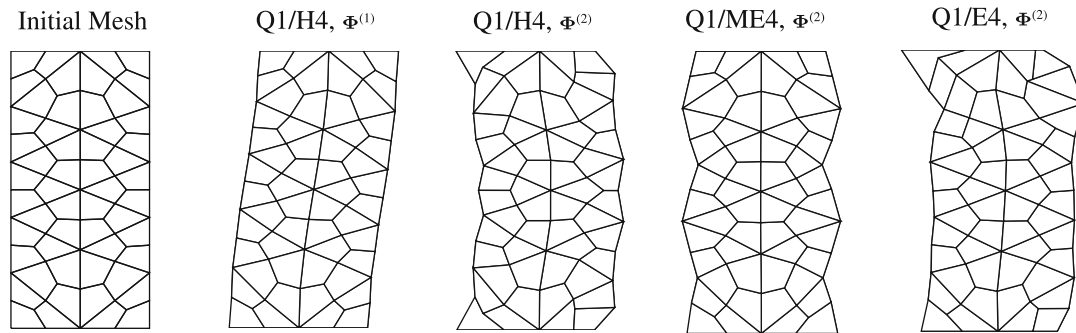
5.3.4 | Mesh distortion

The analysis up to now was restricted to rectangular-shaped elements and the purpose of this test is to cover the case when the mesh is distorted. Figure 11 sketches one of the distorted meshes together with some buckling modes. In contrast to the previous examples, the onset of artificial instabilities are now determined by the individual element, that is most

TABLE 4 Convergence study (cf. Figure 10); critical stretches for two selected uniform meshes

	Ref.	Mesh	Q1	Q1/E4	Q1/ME4	Q1/H4	Q1/MH4-I	Q1/HT4
$\lambda_c^{(1)}$	0.805	4/8	0.759	0.742	0.786	0.793	0.790	0.790
		32/64	0.804	0.805	0.805	0.805	0.805	0.805
$\lambda_c^{(2)}$	0.582	4/8	0.276	0.656*	0.257	0.675*	0.374	0.374
		32/64	0.578	0.656*	0.579	0.675*	0.580	0.580
$\lambda_c^{(3)}$	0.544	4/8	0.245	0.597*	—	0.653*	0.293	0.293
		32/64	0.532	0.654*	0.536	0.669*	0.526	0.538

Note: Values marked with * are afflicted with geometric hourglassing.

**FIGURE 11** Buckling modes superimposed on the undeformed mesh configuration**TABLE 5** Mesh distortion test: critical stretches for $j = 1, 2, 3$

	Ref.	n_{ele}	Q1	Q1/E4	Q1/ME4	Q1/H4	Q1/MH4-I	Q1/HT4
$\lambda_c^{(1)}$	0.805	54	0.757	0.799	0.793	0.801	0.792	0.792
		24	0.709	0.782	0.766	0.782	0.765	0.766
$\lambda_c^{(2)}$	0.582	54	0.193	0.636*	0.490	0.771*	0.447	0.394
		24	0.177	0.682*	0.517	0.647*	0.477	0.449
$\lambda_c^{(3)}$	0.544	54	0.146	0.635*	0.485	0.733*	0.431	0.388
		24	0.142	0.655*	0.491	0.467	0.467	0.449

Note: Values marked with * are afflicted with geometric hourglassing.

prone to become unstable. For the selected cases, no artificial instabilities are observed for the newly proposed elements (cf. Table 5).

5.4 | Material induced instabilities–Tension test

5.4.1 | Setup and reference solution

Inspired by Triantafyllidis et al.,⁶⁰ we consider the special Blatz-Ko rubber for the tension test, such that $\hat{u}_2 > 0$, $P_2 > 0$ and $\lambda_2 > 1$. The analytical solutions for the first four critical stretches are shown in Figure 12 as functions of the block's aspect ratio. For $r \rightarrow 0$ all critical stretches converge towards the value where the $P_2 - \lambda_2$ relation reaches an asymptote (dashed line). For more bulky blocks, the critical stretches are larger. The kinks in the branches result from intersections of solution branches, that is, when the sequence of certain buckling modes, when sorted according to the magnitude of the critical λ_2 , changes. Interestingly, the underlying differential equation remains fully in the elliptic regime, see also Section 3.4.

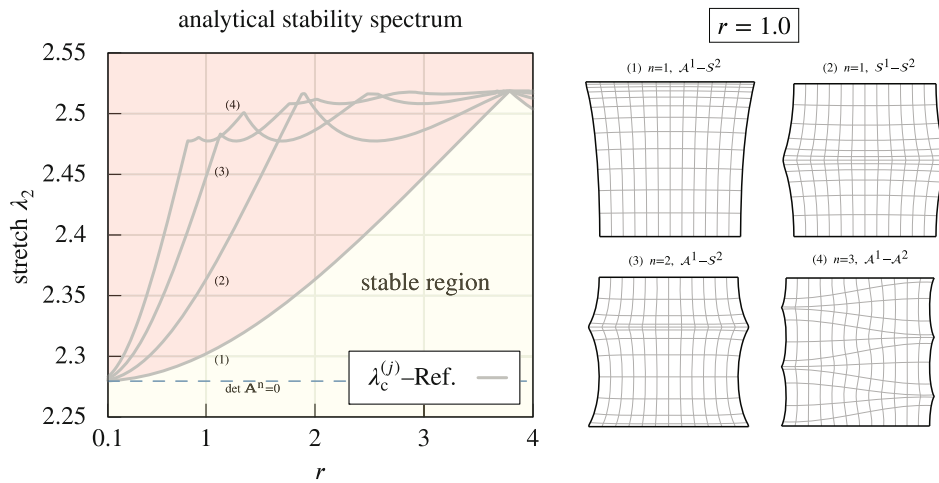


FIGURE 12 Left: Material stability spectrum with analytical solution of the first four bifurcation points, special Blatz-Ko, $E = 1000$, numerical data are provided in Table D1 in Appendix D; right: Contour plot of the first four buckling modes, also called diffuse bifurcation modes, superimposed on the undeformed geometry

TABLE 6 Material hourglassing: Critical stretches for $j = 1, 2, 3$

	Ref.	Mesh	Q2	/E11	/ME11	Q1	/E4	/ME4	/H4	/HT4
$\lambda_c^{(1)}$	2.302	1/1	2.307	1.519*	1.495*	—	1.519*	1.510*	2.306	2.279
		8/8	2.302	1.519*	1.316*	2.313	1.519*	1.509*	2.302	2.279*
$\lambda_c^{(2)}$	2.363	8/8	2.364	1.520*	1.326*	2.414	1.521*	1.511*	2.306*	2.283*
$\lambda_c^{(3)}$	2.447	8/8	2.450	1.522*	1.354*	2.577	1.526*	1.517*	2.310*	2.295*

Note: Values marked with * are afflicted with geometric hourglassing.

5.4.2 | Material hourglassing

All enhanced assumed strain elements fail to reproduce the correct (physical) buckling loads for this simple tension test. The reason for this pathological behavior is material hourglassing.

Table 6 shows analytical and numerical results of the critical stretches for a square block ($r = 1$). In accordance with the results of the modal analysis in Section 3.4, we observe a principally different behavior of the “E” and “H” enhanced formulations. The first ones fail around the stretch state $\lambda_2 = 1.509$ and the latter ones at around $\lambda_2 = 2.279$. These values can be related to the horizontal tangents of the $S_2 - \lambda_2$ - and $P_2 - \lambda_2$ -curves in Figure 3. However, within each of the two classes, minor differences between the individual formulations can be observed, which emanate from different treatment of the geometric stiffness. While Q1/MH4 and Q1/HT4 fail exactly at the stretch value with the horizontal tangent, Q1/E4 as well as Q1/H4 are slightly delayed due to the stabilizing geometric hourglass stiffness.

For the displacement based Q2 element, the upper row of Figure 13 shows the first four critical buckling modes superimposed onto the initial mesh. These modes are in good agreement with the analytical modes sketched in Figure 12. The lower row of Figure 13 sketches typical (material) hourglass patterns for various formulations. Interestingly, the first buckling mode of Q1/H4 (not shown) is a good approximation to the reference solution, the second buckling mode of the Q1/H4 is repeated version of the first mode spoiled with some hourglass patterns. This shows that it is important to consider also higher-order buckling modes for the stability analysis of finite elements.

In summary, we can conclude that, at least for this example, the elements proposed in Section 4, for example, Q1/ME4, as well as the Q1/HT4 perform worse w.r.t material hourglassing. The reason is the absence of the stabilizing geometric hourglass stiffness. In addition, the “nonlinear enhanced” Q1/H4 is superior to the “linear enhanced” Q1/E4 and, although not free of material hourglassing, seems to be more suitable when strong material nonlinearities are involved.

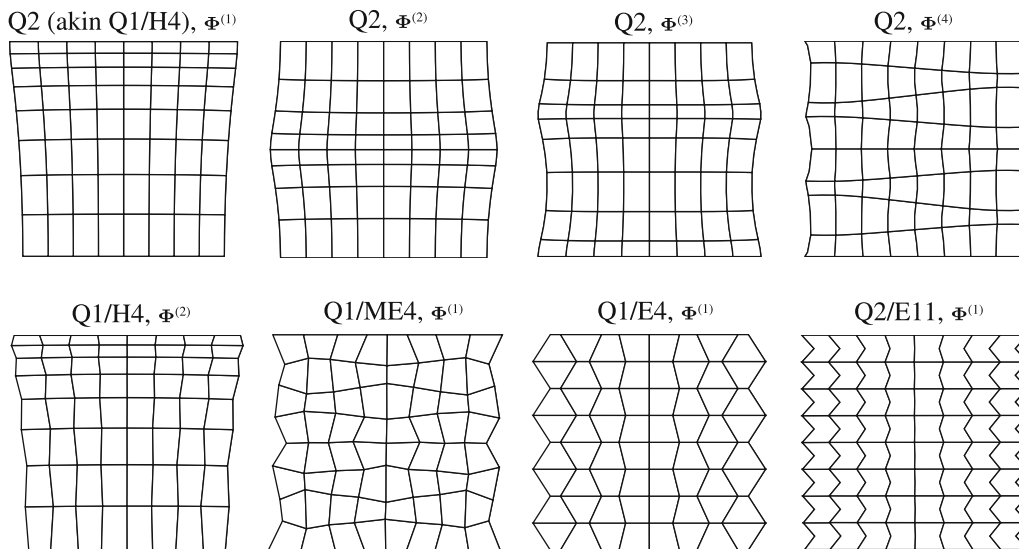


FIGURE 13 Buckling modes superimposed onto the initial mesh configuration; (upper row) approximation with Q2 of the first four buckling modes (the actually curved element edges are not plotted); (lower row) typical hourglass patterns of various EAS formulations

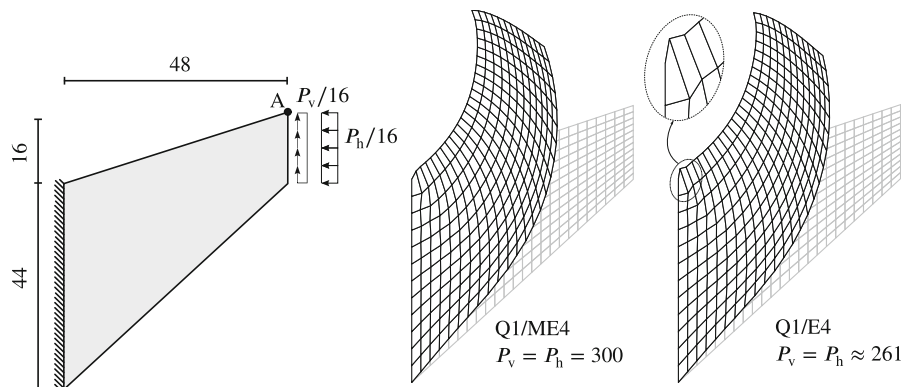


FIGURE 14 Cook's membrane; problem description and two deformed $2m \times m$ ($m = 12$) mesh configurations

6 | FURTHER NUMERICAL EXPERIMENTS

This section analyzes possible consequences of the modification of the Green-Lagrange strain proposed in Section 4. In particular, convergence and stability of the novel elements in comparison with established EAS elements is studied. For this purpose we consider three large strain bending problems. For the sake of brevity, we primarily focus on Q1/ME4. For all simulations the compressible Neo-Hookean strain energy function (61) is used. Furthermore, standard Gauss quadrature, that is, 2×2 for bilinear elements and 3×3 for biquadratic elements, is used.

6.1 | Cook's membrane

This is a well-known benchmark to test element performance in in-plane bending situations. The initial geometry as well as two deformed configurations are depicted in Figure 14. We follow Reference 21 and use a quasi incompressible Neo-Hookean model with Lamé parameters $\Lambda = 400942$ and $\mu = 80.1938$ (Young's modulus $E = 240.5654$ and Poisson's ratio $\nu = 0.4999$). The quantity of interest is the absolute nodal tip displacement $\|\mathbf{d}_A\|$ of the upper right corner for two different scenarios.

First, we consider an $m \times m$ mesh and a vertical loading with a resultant force $P_v = 100$ ($P_h = 0$). Figure 15A shows the convergence plot for various EAS elements. Due to in-plane shear locking, Q1/E2n is stiffer than all other elements. Interestingly, the novel Q1/ME4 element performs slightly more flexible for coarse meshes than the Q1/E4. However, this effect decreases with mesh refinement and all elements converge properly.

For the second scenario we consider a $2m \times m$ mesh in combination with a higher load of $P_v = P_h = 300$, which makes it more challenging with respect to geometric hourglassing. Figure 15B shows that Q1/E4 and Q1/H4 are too flexible for coarse meshes. Moreover, the results become unstable for $m > 10$. In contrast to that, the other elements apparently converge towards the same value. The stress singularity at the top left corner produces potential numerical issues with mesh refinement, but this aspect is not further discussed herein. Figure 14 depicts the deformed meshes for Q1/ME4 as well as Q1/E4. For the latter, the iterations failed to converge after reaching approximately 87% of the target load. The local hourglassing at the upper left corner for Q1/E4 is clearly visible.

6.2 | Pure bending deformations

We next consider the coiling of an initially flat beam-like structure with length $L = 10$ and thickness $T = 2$. A Neo-Hookean material with $E = 100$ and varying Poisson's ratio is considered. The block is clamped at the left end and subjected to two different loading scenarios at the right edge: (i) force control via follower loads and (ii) prescribed rotation angle α , see Figure 16.

We first consider a scenario that uses a $1 \times m$ mesh and $\nu = 0.3$. The structure is subjected to pair of follower loads P_M invoking a bending moment $M = P_M \cdot t = E/15$. Figure 17A shows the absolute tip displacement of point A for an

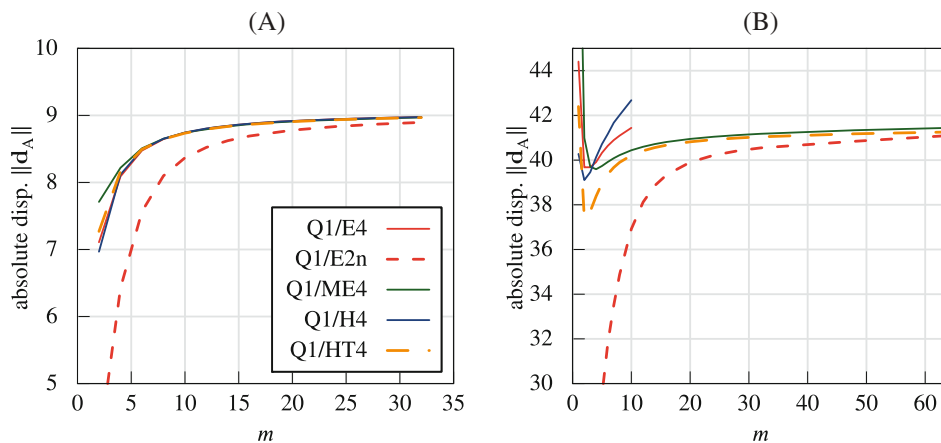


FIGURE 15 Cook's membrane; convergence plot for (A) $P_v = 100, P_h = 0$, uniform $m \times m$ mesh and (B) $P_v = P_h = 300, 2m \times m$ mesh

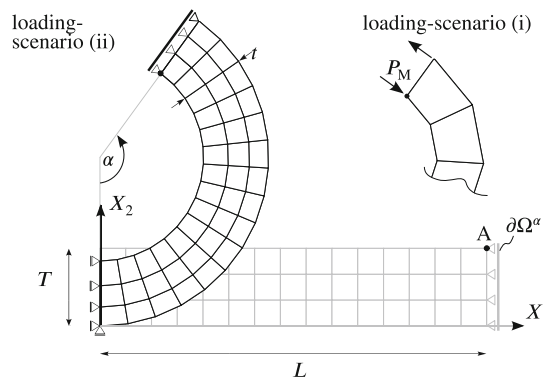


FIGURE 16 Pure bending problem; problem description and deformed 3×15 mesh

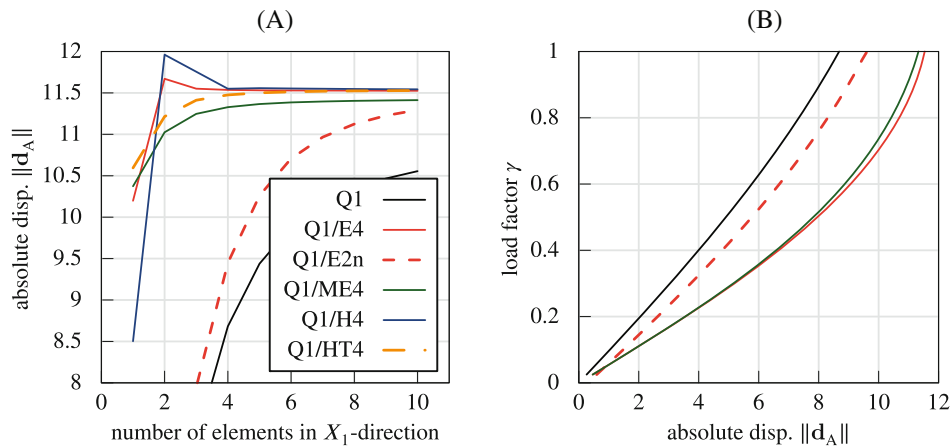


FIGURE 17 Pure bending problem with prescribed $M = E/15$; (A) tip displacement versus number of elements and (B) load-displacement curve for a 1×5 mesh

increasing number of elements in length direction (X_1 -direction). Shear locking for Q1/E2n and in addition (mild) volumetric locking for Q1 yields a stiffer response than the remaining fully locking-free elements. They perform similar, with a slightly stiffer response of Q1/ME4. The reason for this difference is the modification of the hourglass stiffness in combination with the fact that there is no mesh refinement in transverse direction (X_2 -direction). Figure 17B shows the load-displacement curve for a 1×5 mesh, with the load scaled by load factor γ . The results of Q1/ME4 and Q1/E4 coincide at the beginning of the deformation process but deviate when the load is increased and the nonlinear hourglass contributions become more influential. For a similar problem, the slightly stiffer response was also observed by Schwarze and Reese⁶¹ (cf. Sec. 7.4) in the context of a shell formulation where the quadratic Green-Lagrange strain component in thickness direction is neglected.

For the second scenario we consider an $m \times 5m$ mesh, such that the element shapes remain square. A rotation angle $\alpha = \pi$ is prescribed at the right edge along with the constraint of the edge remaining straight. The aim of this second scenario is to show that the novel elements perform well for large bending problems and that the slight deviations from the previous scenario diminishes with mesh refinement in transverse direction. For the incompressible case ($\nu = 0.5$) it is possible to derive an analytical solution for this problem, see Destrade et al.⁶² As a reference we use the variation of the second Piola-Kirchhoff stress component in transverse direction.

$$S_{11} = \frac{157.07963X_2^3 + 217.6835X_2^2 - 114.29004X_2 - 162.05561}{5X_2^2 + 8.79635X_2 + 3.868795}. \quad (66)$$

It is homogeneous in length direction (X_1 -direction), i.e. independent of X_1 . The numerical results for S_{11} in cross sections passing through the Gauss quadrature points, using a quasi incompressible material with $\nu = 0.4999$, is compared to this reference solution. Figure 18 shows the convergence behavior of the relative error

$$e(S_{11}) = \frac{\int_0^T (S_{11} - S_{11}^h)^2 dX_2}{\int_0^T (S_{11})^2 dX_2} \quad (67)$$

versus the number of elements m in X_2 -direction. The integrals in (64) are evaluated with the same Gauss quadrature rule as the element stiffness matrices. For an excellent review on the analytical solution as well as the underlying stability problem, the interested reader is referred to the Secs. 5.5 and 12.4 in Bigoni.⁶³

For coarse meshes Q1/E4 performs slightly better than Q1/ME4 and, interestingly, Q1/HT4 performs slightly better than Q1/H4. With mesh refinement these differences diminish. Almost identical results are observed for Q1/S5 and Q1/MS5 (not shown for the sake of brevity). Qualitatively similar results are also observed for the biquadratic counterparts Q2/E11 and Q2/ME11. The differences are much smaller, though, since the bending problem is dominated by the bilinear (hourglass) strain mode, which is not modified for Q2/ME11.

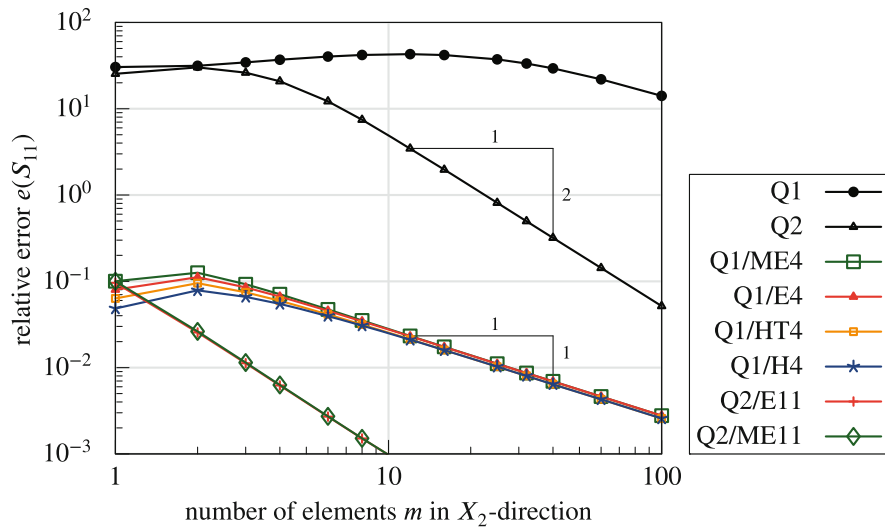


FIGURE 18 Pure bending problem with prescribed $\alpha = \pi$; convergence behavior of various elements. It is remarked that the quasi incompressible simulation does obviously not converge towards the isochoric reference solution with further mesh refinement (the error becomes dominant at around $e \approx 10^{-4}$ for $\nu = 0.4999$)

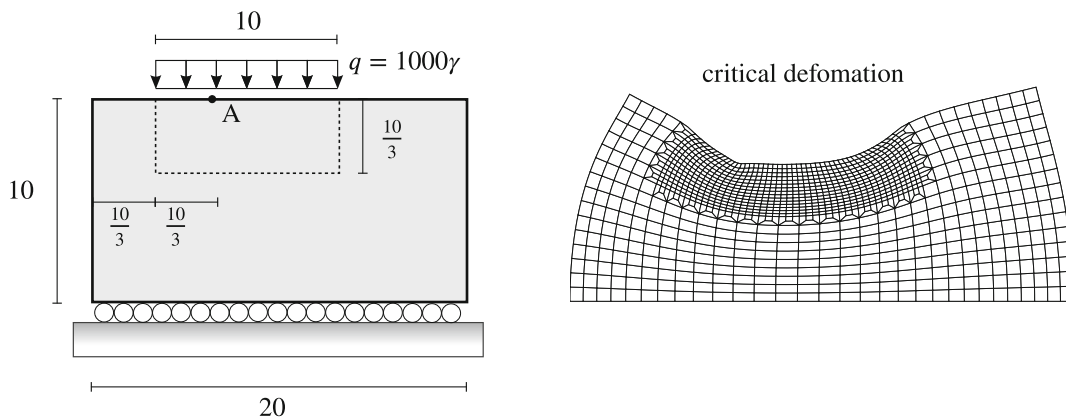


FIGURE 19 Inhomogeneous compression problem; left: problem description; right: deformed mesh at the limit point (Q2, $n_{ele} = 1125$, $\gamma_c = 1.03$)

6.3 | Inhomogeneous compression of a rubber block

For the last benchmark we consider the problem setup shown in Figure 19, see also References 64,65. It consists of a Neo-Hookean block ($E = 1000$, $\nu = 0.49$) subjected to a asymmetrically placed line load q . A load controlled nonlinear analysis is performed with the aim of studying stability of the equilibrium points. Critical points are computed with a combination of accompanying eigenvalue analysis and a bisection algorithm.

The right side of Figure 19 depicts a deformed configuration for a load level at which a (physical) limit point is reached when using Q2 elements. A locally non-smooth deformation pattern near the point marked with A in Figure 19, left, is faintly visible, but it turns out that a finer mesh would be needed to further resolve it. Eventually, the deformation localizes near the point A. For a refined mesh with 1602 elements a limit point is reached with a load factor of $\gamma_c = 1.0215$. This value is considered as a numerical reference solution in the following, without claiming that it is a converged solution.

First, we focus on the coarse mesh accuracy of some selected elements. Figure 20 shows the corresponding load-displacement curves for a uniform 6×3 mesh as well as some deformed mesh configurations. Each of them correspond to the respective final point of the load-displacement curves shown on the left. All simulations with standard EAS elements reach a limit point at around $\gamma_c \approx 1$ (coincidentally, this value is close to the numerical reference

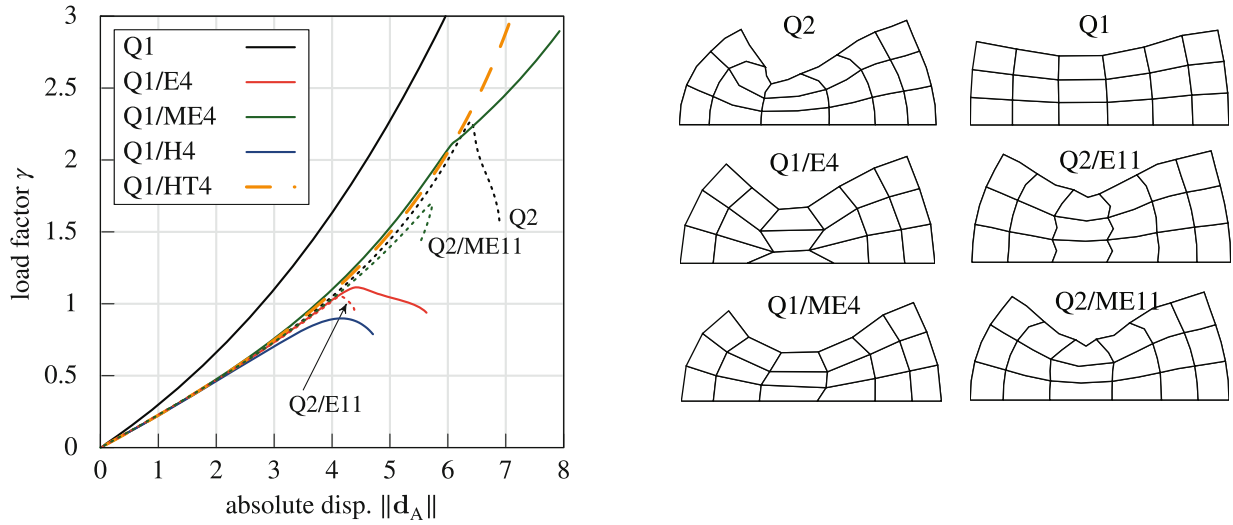


FIGURE 20 Inhomogeneous compression problem; left: load-displacement curves for 3×6 mesh; right: deformed mesh configurations of the final state of the corresponding load-displacement curves

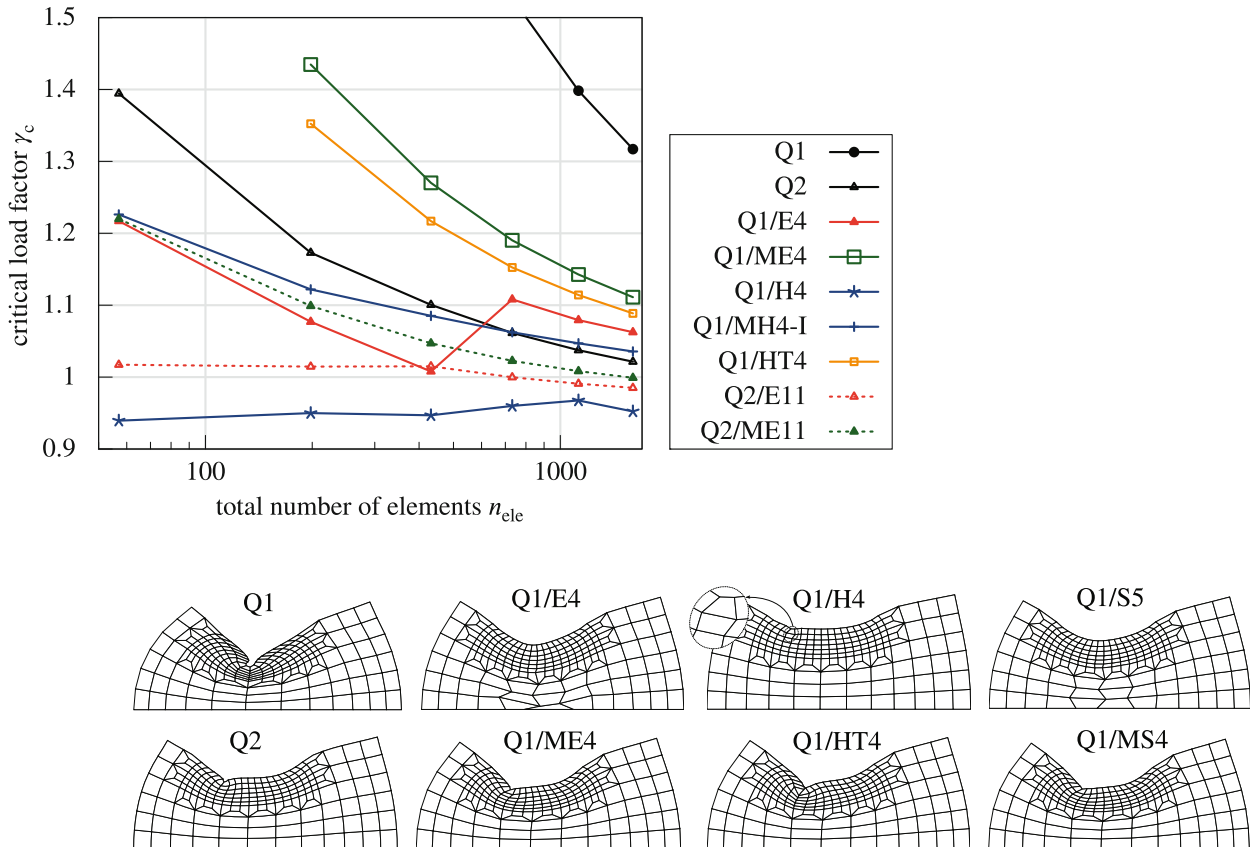


FIGURE 21 Inhomogeneous compression problem; top: critical load factor versus number of elements; bottom: post-critical deformed configurations for $n_{ele} = 198$ (second data-set in graph)

value), but the corresponding buckling modes are obviously dominated by hourglassing, that is, this is not the physically correct critical load. Q1/HT4 is free from hourglassing but fails to reproduce the physical instability. Also Q1/ME4 is free from artificial instabilities but it runs into a stable bifurcation near $\gamma \approx 2.1$. The fact that both elements fail to reproduce the correct physical instability can be explained by the extremely coarse mesh. Only the quadratic elements Q1/ME11 and Q2 are capable of reproducing an approximation of the physical instability mode for this coarse mesh.

We finally consider some refined meshes ($n_{\text{ele}} = \{57, 198, 432, 732, 1125, 1602\}$). The diagram in Figure 21 shows the numerical results for the critical loads plotted versus the number of elements. These computations reveal the difficulties that are often encountered in the distinction between physical and artificial instabilities. As an example, Q1/E4 exhibits geometric hourglassing for the first three meshes and then, coincidentally, accomplishes to capture the limit point, at least visually (not shown). In contrast to that, Q1/H4 fails throughout all simulations in form of local hourglassing, see the enlarged detail. The newly proposed elements as well as Q1/HT4 are free from hourglassing and reproduce a buckling mode that can be considered as likely physical.

7 | CONCLUSIONS

The present study provides new insights into the origin of numerical instabilities observed for various locking-free finite element formulations for nonlinear elasticity, with a focus on Enhanced Assumed Strain (EAS) elements. In particular, the numerical phenomena can be traced back to phenomena that are explainable with classical concepts of stability analysis in structural mechanics. With the help of tailor-made benchmark problems, for which analytical solutions are available, the relationship between element aspect ratio, element formulation and stability properties are systematically described. The results imply a classification of nonlinear hourglassing phenomena into geometric and material hourglassing. Both of them apparently require different strategies to avoid them.

With respect to *geometric* hourglassing, numerical evidence reported in this paper implies that a newly proposed method based on a modification of the computation of the Green Lagrange strain on element level is able to avoid numerical instabilities, while representing physical ones. However, for *material* hourglassing – prominent in problems involving large tensile strains – the newly proposed modification yields even slightly detrimental behavior. The analysis of material hourglassing and corresponding remedies are subject to ongoing research. In this context, both regarding the important distinction between physical and numerical instabilities and the problem of material hourglassing, which strongly depends on the material law, further research is needed to define feasible benchmarks. This does not only apply for stability analysis of finite elements in nonlinear problems but for nonlinear finite element technology in general.

ACKNOWLEDGMENTS

Support for this research was provided by the Deutsche Forschungsgemeinschaft (DFG) under grant BI 722/11-1. Alessandro Reali was partially supported by the Italian Ministry of University and Research (MIUR) through the PRIN project XFAST-SIMS (No. 20173C478N). This support is gratefully acknowledged. Moreover, we thank Robin Pfefferkorn, Tobias Willmann, Alexander Müller and Anton Tkachuk for their valuable comments and helpful discussions. Open Access funding enabled and organized by Projekt DEAL.

CONFLICT OF INTEREST STATEMENT

The authors declare no potential conflict of interests.

DATA AVAILABILITY STATEMENT

The data that support the findings of this study are available from the corresponding author upon reasonable request.

ENDNOTES

*For undistorted elements this is equivalent to the EAS formulation of Simo and Armero.¹² See also the Q1/H4 element in Section 3.3.

†Mostly associated with the lateral geometric stiffness $-P/L$ of an axially loaded column of length L and compression load P .

‡The rigid body rotations are discarded.

§The indicated manipulation with \mathbf{J}_0 (the element's Jacobian $\mathbf{J} = \partial \mathbf{X} / \partial \xi$ at the element center) is necessary to pass the patch test.

¶A special variant of the constitutive relation proposed by Blatz and Ko,⁵⁰ implying $\nu = 1/4$ and $f = 0$, suitable to model for example, foamed polyurethane elastomers.

#Q1 cannot represent constant in-plane bending modes, Q2 is unable to represent linear in-plane bending without artificial strain.

ORCID

Simon Bieber  <https://orcid.org/0000-0001-9669-477X>

REFERENCES

- Zienkiewicz OC, Taylor RL, Too JM. Reduced integration technique in general analysis of plates and shells. *Int J Numer Methods Eng*. 1971;3(2):275-290. doi:10.1002/nme.1620030211
- Bićčanić N, Hinton E. Spurious modes in two-dimensional isoparametric elements. *Int J Numer Methods Eng*. 1979;14(10):1545-1557. doi:10.1002/nme.1620141009
- Kosloff D, Frazier GA. Treatment of hourglass patterns in low order finite element codes. *Int J Numer Anal Methods Geomech*. 1978;2(1):57-72. doi:10.1002/nag.1610020105
- Flanagan DP, Belytschko T. A uniform strain hexahedron and quadrilateral with orthogonal hourglass control. *Int J Numer Methods Eng*. 1981;17(5):679-706. doi:10.1002/nme.1620170504
- Brezzi F. On the existence, uniqueness and approximation of saddle-point problems arising from lagrangian multipliers. *Rev Fr Autom Inform Rec Opér. Anal Numér*. 1974;8:129-151. doi:10.1051/m2an/197408R201291
- Wriggers P, Reese S. A note on enhanced strain methods for large deformations. *Comput Methods Appl Mech Eng*. 1996;135(3):201-209. doi:10.1016/0045-7825(96)01037-7
- de Souza Neto EA, Perić D, Huang GC, Owen DRJ. Remarks on the stability of enhanced strain elements in finite elasticity and elastoplasticity. *Commun Numer Methods Eng*. 1995;11(11):951-961. doi:10.1002/cnm.1640111109
- Reese S, Küssner M, Reddy BD. A new stabilization technique for finite elements in non-linear elasticity. *Int J Numer Methods Eng*. 1999;44(11):1617-1652. doi:10.1002/(SICI)1097-0207(19990420)44:11<1617::AID-NME557%>3.0.CO;2-X
- Reese S. On material and geometrical instabilities in infinite elasticity and elastoplasticity. *Arch Mech*. 2000;52(6):969-999. doi:10.24423/aom.45
- Pfefferkorn R, Betsch P. On transformations and shape functions for enhanced assumed strain elements. *Int J Numer Methods Eng*. 2019;120(2):231-261. doi:10.1002/nme.6133
- Wriggers P. *Nonlinear Finite Element Methods*. Springer; 2008 ISBN 978-3-540-71001-1.
- Simo JC, Armero F. Geometrically non-linear enhanced strain mixed methods and the method of incompatible modes. *Int J Numer Methods Eng*. 1992;33(7):1413-1449. doi:10.1002/nme.1620330705
- Simo JC, Rifai MS. A class of mixed assumed strain methods and the method of incompatible modes. *Int J Numer Methods Eng*. 1990;29(8):1595-1638. doi:10.1002/nme.1620290802
- Wall W, Bischoff M, Ramm E. A deformation dependent stabilization technique, exemplified by EAS elements at large strains. *Comput Methods Appl Mech Eng*. 2000;188(4):859-871. doi:10.1016/S0045-7825(99)00365-5
- Sussman T, Bathe K-J. Spurious modes in geometrically nonlinear small displacement finite elements with incompatible modes. *Comput Struct*. 2014;140:14-22. doi:10.1016/j.compstruc.2014.04.004
- Armero F. On the locking and stability of finite elements in finite deformation plane strain problems. *Comput Struct*. 2000;75(3):261-290. doi:10.1016/S0045-7949(99)00136-4
- Viebahn N, Schröder J, Wriggers P. An extension of assumed stress finite elements to a general hyperelastic framework. *Adv Model Simul Eng Sci*. 2019;6(1):9. doi:10.1186/s40323-019-0133-z
- Reese S, Wriggers P. A stabilization technique to avoid hourglassing in finite elasticity. *Int J Numer Methods Eng*. 2000;48(1):79-109. doi:10.1002/(SICI)1097-0207(20000510)48:1<79::AID-NME869>3.0.CO;2-D
- Auricchio F, Beirão da Veiga L, Lovadina C, Reali A, Taylor RL, Wriggers P. Approximation of incompressible large deformation elastic problems: some unresolved issues. *Comput. Mech*. 2013;52(5):1153-1167. doi:10.1007/s00466-013-0869-0
- Korelc J, Wriggers P. Consistent gradient formulation for a stable enhanced strain method for large deformations. *Eng Comput*. 1996;13(1):103-123. doi:10.1108/02644409610111001
- Glaser S, Armero F. On the formulation of enhanced strain finite elements in finite deformations. *Eng Comput*. 1997;14(7):759-791. doi:10.1108/02644409710188664
- Nadler B, Rubin MB. A new 3-d finite element for nonlinear elasticity using the theory of a cosserat point. *Int J Solids Struct*. 2003;40(17):4585-4614. doi:10.1016/S0020-7683(03)00210-5
- Mueller-Hoeppe DS, Loehnert S, Wriggers P. A finite deformation brick element with inhomogeneous mode enhancement. *Int J Numer Methods Eng*. 2009;78(10):1164-1187. doi:10.1002/nme.2523
- Schröder J, Viebahn N, Wriggers P, Auricchio F, Steeger K. On the stability analysis of hyperelastic boundary value problems using three- and two-field mixed finite element formulations. *Comput. Mech*. 2017;60(3):479-492. doi:10.1007/s00466-017-1415-2
- Krischok A, Linder C. On the enhancement of low-order mixed finite element methods for the large deformation analysis of diffusion in solids. *Int J Numer Methods Eng*. 2016;106(4):278-297. doi:10.1002/nme.5120
- Neunteufel M, Pechstein AS, Schöberl J. Three-field mixed finite element methods for nonlinear elasticity. *Comput Methods Appl Mech Eng*. 2021;382:113857. doi:10.1016/j.cma.2021.113857
- Bayat HR, Krämer J, Wunderlich L, et al. Numerical evaluation of discontinuous and nonconforming finite element methods in nonlinear solid mechanics. *Comput Mech*. 2018;62:1413-1427. doi:10.1007/s00466-018-1571-z
- Schröder J, Wriggers P, Balzani D. A new mixed finite element based on different approximations of the minors of deformation tensors. *Comput Methods Appl Mech Eng*. 2011;200(49):3583-3600. doi:10.1016/j.cma.2011.08.009

29. Bonet J, Gil AJ, Ortigosa R. A computational framework for polyconvex large strain elasticity. *Comput Methods Appl Mech Eng*. 2015;283:1061-1094. doi:[10.1016/j.cma.2014.10.002](https://doi.org/10.1016/j.cma.2014.10.002)
30. Petryk H. Theory of material instability in incrementally nonlinear plasticity. In: Petryk H, ed. *Material Instabilities in Elastic and Plastic Solids*. Springer; 2000:261-331. doi:[10.1007/978-3-7091-2562-5_5](https://doi.org/10.1007/978-3-7091-2562-5_5)
31. Chen G, Baker G. Material softening and structural instability. *Adv Struct Eng*. 2003;6(4):353-357. doi:[10.1260/136943303322771727](https://doi.org/10.1260/136943303322771727)
32. Simo JC, Armero F, Taylor RL. Improved versions of assumed enhanced strain tri-linear elements for 3d finite deformation problems. *Comput Methods Appl Mech Eng*. 1993;110(3):359-386. doi:[10.1016/0045-7825\(93\)90215-J](https://doi.org/10.1016/0045-7825(93)90215-J)
33. de Souza Neto EA, Perić D, Dutko M, Owen DRJ. Design of simple low order finite elements for large strain analysis of nearly incompressible solids. *Int J Solids Struct*. 1996;33(20):3277-3296. doi:[10.1016/0020-7683\(95\)00259-6](https://doi.org/10.1016/0020-7683(95)00259-6)
34. Crisfield MA, Norris V. A stabilised large-strain elasto-plastic Q1-P0 method. *Int J Numer Methods Eng*. 1999;46(4):579-592. doi:[10.1002/\(SICI\)1097-0207\(19991010\)46:4<579::AID-NME689>3.0.CO;2-1](https://doi.org/10.1002/(SICI)1097-0207(19991010)46:4<579::AID-NME689>3.0.CO;2-1)
35. Auricchio F, Beirão da Veiga L, Lovadina C, Reali A. A stability study of some mixed finite elements for large deformation elasticity problems. *Comput Methods Appl Mech Eng*. 2005;194(9):1075-1092. doi:[10.1016/j.cma.2004.06.014](https://doi.org/10.1016/j.cma.2004.06.014)
36. Simo JC, Taylor RL, Pister KS. Variational and projection methods for the volume constraint in finite deformation elasto-plasticity. *Comput Methods Appl Mech Eng*. 1985;51(1):177-208. doi:[10.1016/0045-7825\(85\)90033-7](https://doi.org/10.1016/0045-7825(85)90033-7)
37. Hille M, Pfefferkorn R, Betsch P. Locking-free mixed finite element methods and their spurious hourglass patterns. In: Aldakheel F, Hudobivnik B, Soleimani M, Wessels H, Weißenfels C, Marino M, eds. *Current Trends and Open Problems in Computational Mechanics*. Springer; 2022. doi:[10.1007/978-3-030-87312-7_19](https://doi.org/10.1007/978-3-030-87312-7_19)
38. Willmann T, Bieber S, Bischoff M. Investigation and elimination of nonlinear poisson stiffening in 3d and solid shell finite elements. *Int J Numer Methods Eng*. 2022;124(1):235-263. doi:[10.1002/nme.7119](https://doi.org/10.1002/nme.7119)
39. Areias PMA, César de Sá JMA, Conceição António CA, Fernandes AA. Analysis of 3d problems using a new enhanced strain hexahedral element. *Int J Numer Methods Eng*. 2003;58(11):1637-1682. doi:[10.1002/nme.835](https://doi.org/10.1002/nme.835)
40. Korelc J, Šolinc U, Wriggers P. An improved EAS brick element for finite deformation. *Comput. Mech*. 2010;46(4):641-659. doi:[10.1007/s00466-010-0506-0](https://doi.org/10.1007/s00466-010-0506-0)
41. Reese S. On a consistent hourglass stabilization technique to treat large inelastic deformations and thermo-mechanical coupling in plane strain problems. *Int J Numer Methods Eng*. 2003;57(8):1095-1127. doi:[10.1002/nme.719](https://doi.org/10.1002/nme.719)
42. Wilson EL, Taylor RL, Doherty WP, Ghaboussi J. Incompatible displacement models. In: Fenves SJ, Perrone N, Robinson AR, Schnobrich WC, eds. *Numerical and Computer Methods in Structural Mechanics*. Academic Press; 1973:43-57. doi:[10.1016/B978-0-12-253250-4.50008-7](https://doi.org/10.1016/B978-0-12-253250-4.50008-7)
43. Hjelmstad KJ. *Fundamentals of Structural Mechanics*. second ed. Springer; 2005 ISBN 3-030-89943-8.
44. Holzapfel GA. *Nonlinear Solid Mechanics: A Continuum Approach for Engineering*. Wiley; 2010 ISBN 0-471-82319-8.
45. Betsch P, Gruttmann F, Stein E. A 4-node finite shell element for the implementation of general hyperelastic 3d-elasticity at finite strains. *Comput Methods Appl Mech Eng*. 1996;130(1):57-79. doi:[10.1016/0045-7825\(95\)00920-5](https://doi.org/10.1016/0045-7825(95)00920-5)
46. Bischoff M, Ramm E. Shear deformable shell elements for large strains and rotations. *Int J Numer Methods Eng*. 1997;40(23):4427-4449. doi:[10.1002/\(SICI\)1097-0207\(19971215\)40:23<4427::AID-NME268%>3.0.CO;2-9](https://doi.org/10.1002/(SICI)1097-0207(19971215)40:23<4427::AID-NME268%>3.0.CO;2-9)
47. Klinkel S, Wagner W. A geometrical non-linear brick element based on the EAS-method. *Int J Numer Methods Eng*. 1997;40(24):4529-4545. doi:[10.1002/\(SICI\)1097-0207\(19971230\)40:24<4529::AID-NME271%>3.0.CO;2-I](https://doi.org/10.1002/(SICI)1097-0207(19971230)40:24<4529::AID-NME271%>3.0.CO;2-I)
48. Crisfield MA, Moita GF, Lyons LPR, Jelenić G. Enhanced lower-order element formulations for large strains. *Comput. Mech*. 1995;17(1):62-73. doi:[10.1007/BF00356479](https://doi.org/10.1007/BF00356479)
49. Pfefferkorn R, Betsch P. Hourglassing- and locking-free mesh distortion insensitive petrov-galerkin eas elements for large deformation solid mechanics. *Int J Numer Methods Eng*. 2022;124(6):1307-1343. Accepted.
50. Blatz PJ, Ko WL. Application of finite elastic theory to the deformation of rubbery materials. *Trans Soc Rheol*. 1962;6(1):223-252. doi:[10.1122/1.548937](https://doi.org/10.1122/1.548937)
51. Knowles JK, Sternberg E. On the ellipticity of the equations of nonlinear elastostatics for a special material. *J Elast*. 1975;5(3):341-361. doi:[10.1007/BF00126996](https://doi.org/10.1007/BF00126996)
52. Horgan CO. Remarks on ellipticity for the generalized blatz-ko constitutive model for a compressible nonlinearly elastic solid. *J Elast*. 1996;42(2):165-176. doi:[10.1007/BF00040959](https://doi.org/10.1007/BF00040959)
53. Pian THH, Sumihara K. Rational approach for assumed stress finite elements. *Int J Numer Methods Eng*. 1984;20(9):1685-1695. doi:[10.1002/nme.1620200911](https://doi.org/10.1002/nme.1620200911)
54. Pfefferkorn R, Bieber S, Oesterle B, Bischoff M, Betsch P. Improving efficiency and robustness of enhanced assumed strain elements for nonlinear problems. *Int J Numer Methods Eng*. 2021;122(8):1911-1939. doi:[10.1002/nme.6605](https://doi.org/10.1002/nme.6605)
55. Wagner W, Wriggers P. A simple method for the calculation of postcritical branches. *Eng Comput*. 1988;5(2):103-109. doi:[10.1108/eb023727](https://doi.org/10.1108/eb023727)
56. Roth S. *Algorithmen Zur Nichtlinearen Stabilitätsanalyse Dünnwandiger Strukturen*. Dissertation. Universität Stuttgart; 2020 ISBN 978-3-00-067327-6, <https://elib.uni-stuttgart.de/handle/11682/11256>
57. Hughes TJR. *The Finite Element Method: Linear Static and Dynamic Finite Element Analysis*. Dover Publications Inc.; 2012 ISBN 0-486-41181-8.
58. Lesaint P. On the convergence of wilson's nonconforming element for solving the elastic problems. *Comput Methods Appl Mech Eng*. 1976;7(1):1-16. doi:[10.1016/0045-7825\(76\)90002-5](https://doi.org/10.1016/0045-7825(76)90002-5)
59. Reddy BD, Simo JC. Stability and convergence of a class of enhanced strain methods. *SIAM J Numer Anal*. 1995;32(6):1705-1728. doi:[10.1137/0732077](https://doi.org/10.1137/0732077)

60. Triantafyllidis N, Scherzinger WM, Huang HJ. Post-bifurcation equilibria in the plane-strain test of a hyperelastic rectangular block. *Int J Solids Struct.* 2007;44(11):3700-3719. doi:10.1016/j.ijsolstr.2006.10.012
61. Schwarze M, Reese S. A reduced integration solid-shell finite element based on the EAS and the ANS concept—large deformation problems. *Int J Numer Methods Eng.* 2011;85(3):289-329. doi:10.1002/nme.2966
62. Destrade M, Gilchrist MD, Murphy JG. Onset of nonlinearity in the elastic bending of blocks. *J Appl Mech.* 2010;77(6):061015-1 - 061015-6. doi:10.1115/1.4001282
63. Bigoni D. *Nonlinear Solid Mechanics: Bifurcation Theory and Material Instability.* Cambridge University Press; 2012.
64. Bischoff M, Bletzinger K-U. Interaction of locking and element stability at large strains. In: Owen DRJ, Onate E, Suarez B, eds. *VIII International Conference on Computational Plasticity. CIMNE*; 2005 ISBN 9788495999801.
65. Ko Y, Bathe K-J. A new 8-node element for analysis of three-dimensional solids. *Comput Struct.* 2018;202:85-104. doi:10.1016/j.compstruc.2018.02.015
66. Biot MA. *Mechanics of Incremental Deformations.* John Wiley and Sons; 1965 ISBN 0-471-07310-5.
67. Hill R, Hutchinson JW. Bifurcation phenomena in the plane tension test. *J Mech Phys Solids.* 1975;23(4):239-264. doi:10.1016/0022-5096(75)90027-7
68. Young NJB. Bifurcation phenomena in the plane compression test. *J Mech Phys Solids.* 1976;24(1):77-91. doi:10.1016/0022-5096(76)90019-3
69. Ogden RW. *Non-linear Elastic Deformations.* Dover Publications Inc.; 1997 ISBN 0-486-69648-0.

How to cite this article: Bieber S, Auricchio F, Reali A, Bischoff M. Artificial instabilities of finite elements for nonlinear elasticity: Analysis and remedies. *Int J Numer Methods Eng.* 2023;124(11):2638-2675. doi:10.1002/nme.7224

APPENDIX A. LINEARIZED STIFFNESS MATRIX

A.1 Based on the “Wilson modes” (Q1/H4)

In compact matrix notation the stiffness matrices derived in Section 2.1 can be computed via

$$\mathbf{K}_e = \int_{\Omega} \mathbf{B}_H^T \mathbf{A}_e \mathbf{B}_H \, dA \quad \text{and} \quad \mathbf{K}_g = \int_{\Omega} \mathbf{B}_H^T \mathbf{A}_g \mathbf{B}_H \, dA \quad (\text{A1})$$

with modal strain-displacement operator

$$\mathbf{B}_H = \begin{bmatrix} 1/L_1 & 0 & 0 & 0 & \eta/L_1 & 0 & 0 & 0 \\ 0 & 1/L_2 & 0 & 0 & 0 & \xi/L_2 & 0 & 0 \\ 0 & 0 & 1/L_2 & 0 & \xi/L_2 & 0 & \eta/L_2 & 0 \\ 0 & 0 & 0 & 1/L_1 & 0 & \eta/L_1 & 0 & \xi/L_1 \end{bmatrix}, \quad (\text{A2})$$

associated with displacement gradient $(H_{11}, H_{22}, H_{12}, H_{21})^T$ and displacement ansatz (2). The general material matrix and stress matrix read

$$\mathbf{A}_e = \begin{bmatrix} \Lambda + 2G & \Lambda & 0 & 0 \\ \Lambda & \Lambda + 2G & 0 & 0 \\ 0 & 0 & G & G \\ 0 & 0 & G & G \end{bmatrix} \quad \text{and} \quad \mathbf{A}_g = \begin{bmatrix} \sigma_{11} & 0 & 0 & 0 \\ 0 & \sigma_{22} & 0 & 0 \\ 0 & 0 & \sigma_{22} & 0 \\ 0 & 0 & 0 & \sigma_{11} \end{bmatrix}, \quad (\text{A3})$$

respectively, with elastic constants $\Lambda = G(E - 2G)/(3G - E)$. This yields, with $\Lambda = \nu = 0$, $E = 2G$ and stress state $\boldsymbol{\sigma} = \text{diag}(0, -\gamma p)$ the elastic stiffness (3) as well as the geometric stiffness matrix (5).

Static condensation of parameters c_{7-8} from $\mathbf{K}^1 = \mathbf{K}_e^1 + \mathbf{K}_g^1$ (cf. Equations (3) and (5)) provides the stiffness matrix

$$\mathbf{K}_{\text{red}}^1 = \begin{bmatrix} \frac{E}{3r_e} + \frac{Gr_e}{3} + \frac{\sigma_{22}r_e}{3} & 0 \\ 0 & \frac{Er_e}{3} + \frac{G}{3r_e} + \frac{\sigma_{22}r_e}{3} \end{bmatrix} - \underbrace{\begin{bmatrix} \frac{Gr_e}{3} & 0 \\ 0 & \frac{G^2}{3r_e(G+\sigma_{22})} \end{bmatrix}}_{\text{EAS contribution}}. \quad (\text{A4})$$

Here, the second diagonal term can be written as a power series in σ_{22} as

$$K_{\text{red}}^{66} = \frac{Er_e}{3} + \frac{1}{3} \frac{r_e^2 + 1}{r_e} \sigma_{22} + \frac{1}{3r_e} \sum_{n=1}^{\infty} \frac{(-2)^n}{E^n} (\sigma_{22})^{n+1}, \quad (\text{A5})$$

where for small ratios σ_{22}/E , the last term may be neglected and approximation (10) is recovered, making it more accessible for a physical interpretation.

A.2 Based on the “transposed Wilson modes” (Q1/HT4)

The corresponding stiffness matrix is obtained by a modified \mathbf{B}_H -operator which is obtained by switching the terms in the last two rows of Equation (A2). Static condensation of c_{7-8} yields

$$\mathbf{K}_{\text{red}}^1 = \begin{bmatrix} \frac{E}{3r_e} + \frac{Gr_e}{3} + \frac{\sigma_{22}r_e}{3} & 0 \\ 0 & \frac{Er_e}{3} + \frac{G}{3r_e} + \frac{\sigma_{22}r_e}{3} \end{bmatrix} - \underbrace{\begin{bmatrix} \frac{Gr_e}{3} + \frac{\sigma_{22}r_e}{3} & 0 \\ 0 & \frac{G}{3r_e} \end{bmatrix}}_{\text{EAS contribution}} \quad (\text{A6})$$

and recovers Equation (9).

APPENDIX B. MODAL ANALYSIS

Relation between \mathbf{A} and \mathbf{C} is given by

$$\mathbf{A} = \begin{bmatrix} A_{11}^n & A_{12}^n & 0 & 0 \\ A_{12}^n & A_{22}^n & 0 & 0 \\ 0 & 0 & A_{11}^s & A_{12}^s \\ 0 & 0 & A_{12}^s & A_{22}^s \end{bmatrix} = \begin{bmatrix} \lambda_1^2 C_{11}^n + S_1 & \lambda_1 \lambda_2 C_{12}^n & 0 & 0 \\ \lambda_1 \lambda_2 C_{12}^n & \lambda_2^2 C_{22}^n + S_2 & 0 & 0 \\ 0 & 0 & \lambda_1^2 C_{12}^s + S_2 & \lambda_1 \lambda_2 C_{12}^s \\ 0 & 0 & \lambda_1 \lambda_2 C_{12}^s & \lambda_2^2 C_{12}^s + S_1 \end{bmatrix}. \quad (\text{B1})$$

For the strain energy function (41) of the Blatz-Ko rubber, the corresponding coefficients of the elastic moduli \mathbb{C} are given as

$$\begin{aligned} C_{11}^n &= \mathbb{C}_{1111} = \mu \left(\frac{4}{\lambda_1^6} - \frac{\lambda_2}{\lambda_1^3} \right), & C_{22}^n &= \mathbb{C}_{2222} = \mu \left(\frac{4}{\lambda_2^6} - \frac{\lambda_1}{\lambda_2^3} \right), \\ C_{12}^n &= \mathbb{C}_{1122} = \mu \left(\frac{1}{\lambda_1 \lambda_2} \right), & C_{12}^s &= \mathbb{C}_{1221} = \mu \left(-\frac{1}{\lambda_1 \lambda_2} + \frac{1}{\lambda_1^2 \lambda_2^4} + \frac{1}{\lambda_1^4 \lambda_2^2} \right). \end{aligned} \quad (\text{B2})$$

APPENDIX C. IMPLEMENTATION

At element node A , the shape function N^A and its material gradient $\nabla N^A = \text{Grad} N^A$ is used to express the compatible displacement gradient and variation of the Green-Lagrange strain as

$$\mathbf{H} = \sum_A^{n_{\text{no}}} \mathbf{d}^A \otimes \nabla N^A \quad \text{and} \quad \delta \mathbf{E} = \sum_A^{n_{\text{no}}} \mathbf{B}^A \delta \mathbf{d}^A. \quad (\text{C1})$$

Here, the “standard” nodal B-operator reads

$$\mathbf{B}^A := \mathbf{B}_{\text{no}}(\mathbf{F}, \nabla N^A) = \begin{bmatrix} F_{11} N_{,1}^A & F_{21} N_{,1}^A \\ F_{12} N_{,2}^A & F_{22} N_{,2}^A \\ F_{12} N_{,1}^A + F_{11} N_{,2}^A & F_{21} N_{,2}^A + F_{22} N_{,1}^A \end{bmatrix}. \quad (\text{C2})$$

Furthermore, we obtain the “standard” geometric operator (22) for node A and B via

$$[\mathbb{G}^{\text{dd}}]^{AB} := \mathbb{G}_{\text{no}}^{\text{dd}}(\mathbf{S}, \nabla N^A, \nabla N^B) = (\nabla N^A)^T \mathbf{S} \nabla N^B \cdot \mathbf{1}, \quad (\text{C3})$$

with $\mathbf{S} = \mathbf{S}(\mathbf{E})$.

A possible way to implement the principle idea of Section 4 is to *subtract* the undesired terms from *existing* (“standard”) quantities. The modified strain expression in Equation (50) can then be expressed as $\dot{\mathbf{E}} = \mathbf{E} - \frac{1}{2} \mathbf{H}_h^T \mathbf{H}_h$. In correspondence with the split of the displacement gradient we introduce $\mathbf{N} = \mathbf{N}_r + \mathbf{N}_h$. Assuming that $\dot{\mathbf{d}} = \mathbf{d}$ (EAS parts are not altered), the modified operators in (48) read

$$\dot{\mathbf{B}}^A := \mathbf{B}^A - \mathbf{B}_{\text{no}}(\mathbf{H}_h, \text{Grad} N_h^A) \quad \text{and} \quad [\dot{\mathbb{G}}^{\text{dd}}]^{AB} := [\mathbb{G}^{\text{dd}}]^{AB} - \mathbb{G}_{\text{no}}^{\text{dd}}(\mathbf{S}, \nabla N_h^A, \nabla N_h^B), \quad (\text{C4})$$

with $\mathbf{S} = \mathbf{S}(\dot{\mathbf{E}})$. Exemplified for the modified strain expression (51) of Q1/ME4, the terms which have to be subtracted read

$$\mathbf{B}_{\text{no}}(\mathbf{H}_h, \text{Grad} N_h^A) = \begin{bmatrix} H_{1|11} N_{1,1}^A & H_{1|12} N_{1,1}^A \\ H_{1|12} N_{1,2}^A & H_{1|22} N_{1,2}^A \\ H_{1|12} N_{1,1}^A + H_{1|11} N_{1,2}^A & H_{1|21} N_{1,2}^A + H_{1|22} N_{1,1}^A \end{bmatrix} \quad (\text{C5})$$

and

$$\mathbb{G}_{\text{no}}^{\text{dd}}(\mathbf{S}, \nabla N_h^A, \nabla N_h^B) = (\nabla N_h^A)^T \mathbf{S}(\dot{\mathbf{E}}) \nabla N_h^B \cdot \mathbf{1}. \quad (\text{C6})$$

Here $N_1^A = N^A - N_0^A$, with $N_0^A = N^A \Big|_{\xi=0}$, denotes the non-constant part of the standard bilinear shape functions and $\mathbf{S} = \mathbf{S}(\dot{\mathbf{E}}^c + \dot{\mathbf{E}})$.

APPENDIX D. ANALYTICAL SOLUTION OF THE BIFURCATION PROBLEM

The theoretical analysis is based on the pioneering work of Biot.⁶⁶ A more general treatment can be found in Hill and Hutchinson⁶⁷ and Young,⁶⁸ for the tension case and compression case, respectively, see also Chap. 6.3 of Ogden.⁶⁹ In the following we provide a short sketch of the solution. The notation is adopted from the readable paper of Triantafyllidis et al.⁶⁰

Starting point for the analytical solution is the Euler-Lagrange equation of bifurcation criterion (59)

$$\boxed{\text{Div}(\mathbb{A}(\mathbf{u}_0, \lambda_c) : \text{Grad} \Delta \mathbf{u}) = 0} \quad (\text{D1})$$

This yields the characteristic equation

$$a \Delta u_{i,1111} + b \Delta u_{i,1122} + c \Delta u_{i,2222} = 0, \quad (\text{D2})$$

with $i = 1, 2$ and coefficients (related to the elasticity tensor \mathbb{A})

$$a := A_{1111} A_{1212}, \quad 2b := A_{1111} A_{2222} + A_{1212} A_{2121} - (A_{1122} A_{2112})^2, \quad c := A_{2222} A_{2121}. \quad (\text{D3})$$

Equation (D1) and the corresponding incremental boundary conditions (cf. Section 5.2) can be satisfied by the ansatz

$$S^1 \begin{cases} \Delta u_1 = v_1(p_1 X_1) \cos(p_2 X_2) \\ \Delta u_2 = -v_2(p_1 X_1) \sin(p_2 X_2) \\ p_2 = n\pi/L_2 \end{cases} \quad \text{or} \quad A^1 \begin{cases} \Delta u_1 = v_1(p_1 X_1) \sin(p_2 X_2) \\ \Delta u_2 = -v_2(p_1 X_1) \cos(p_2 X_2) \\ p_2 = \left(n - \frac{1}{2}\right) \pi/L_2 \end{cases} \quad (\text{D4})$$

with positive integers n . Here S^1/\mathcal{A}^1 and (later) S^2/\mathcal{A}^2 designate the symmetric/antisymmetric modes w.r.t the X_1 - and X_2 -axis. Inserting ansatz (D3) in (D1) yields the characteristic equation

$$a\left(\frac{p_1}{p_2}\right)^4 + b\left(\frac{p_1}{p_2}\right)^2 + c = 0, \quad (\text{D5})$$

with the four solutions

TABLE D1 Critical stretches $\lambda_2 = \lambda_c^{(j)}$; left: compression problem of a Neo-Hookean block with $\nu = 0.45$ and strain energy function (61); right: tension problem of a Blatz-Ko block, with strain energy function (41)

\mathbf{r}	$\lambda_c^{(1)}$	$\lambda_c^{(2)}$	$\lambda_c^{(3)}$	$\lambda_c^{(4)}$
Neo-Hooke – compression				
0.1000	0.9917	0.9672	0.9268	0.8718
0.1258	0.9869	0.9482	0.8852	0.8031
0.1584	0.9794	0.9185	0.8225	0.7149
0.1995	0.9674	0.8724	0.7376	0.6338
0.2511	0.9485	0.8039	0.6516	0.5820
0.3162	0.9189	0.7158	0.5922	0.5546
0.3981	0.8730	0.6345	0.5598	0.5419
0.5011	0.8048	0.5824	0.5442	0.5370
0.6309	0.7167	0.5548	0.5378	0.5356
0.7943	0.6352	0.5420	0.5358	0.5352
1.0000	0.5828	0.5371	0.5353	0.5352
1.2589	0.5550	0.5356	0.5352	0.5352
1.5848	0.5421	0.5353	0.5352	0.5352
1.9952	0.5371	0.5352	0.5352	0.5352
2.5118	0.5356	0.5352	0.5352	0.5352
3.1622	0.5353	0.5352	0.5352	0.5352
3.9810	0.5352	0.5352	0.5352	0.5352
5.0118	0.5352	0.5352	0.5352	0.5352
6.3095	0.5352	0.5352	0.5352	0.5352
7.9432	0.5352	0.5352	0.5352	0.5352
10.000	0.5352	0.5352	0.5352	0.5352
Special Blatz-Ko – tension				
0.1	2.2797	2.2804	2.2815	2.2831
0.5	2.2852	2.3020	2.3287	2.3633
1.0	2.3020	2.3633	2.4479	2.4775
1.5	2.3287	2.4479	2.4838	2.4864
2.0	2.3633	2.4864	2.5037	2.5116
2.5	2.4038	2.4775	2.5116	2.5162
3.0	2.4479	2.4864	2.5082	2.5168
3.5	2.4932	2.5070	2.5143	2.5173
4.0	2.5037	2.5126	2.5168	2.5182

$$\left(\frac{p_1}{p_2}\right)^2 = \frac{-b \pm \sqrt{b^2 - ac}}{a} \quad \Rightarrow p_1 = p_2 \{\pm i\alpha, \pm i\beta\}, \quad (\text{D6})$$

where $i = \sqrt{-1}$ denotes the imaginary unit. We are only interested in the elliptic domain, that is, where ellipticity of Equation (D1) holds. This implies $a > 0, c > 0, b > -\sqrt{ac}$ (cf. Sec. 6.2.7 in Reference 69) and yields the distinction between two different cases:

- Elliptic-imaginary (EI) solutions with $b > \sqrt{ac}$ and real α, β (cf. Case 1 in Reference 69, p. 417).
- Elliptic-complex (EC) solutions with $b < \sqrt{ac}$ and complex conjugates $\alpha = \gamma + i\delta$ and $\beta = \gamma - i\delta$ (cf. Case 3 in Reference 69, p. 418).

This requires a X_1 -dependent ansatz of the form

$$\mathcal{S}^2 \begin{cases} v_1 = A_1 s_\alpha + B_1 s_\beta \\ v_2 = A_2 c_\alpha + B_2 c_\beta \end{cases} \quad \text{or} \quad \mathcal{A}^2 \begin{cases} v_1 = C_1 c_\alpha + D_1 c_\beta \\ v_2 = C_2 s_\alpha + D_2 s_\beta \end{cases} \quad (\text{D7})$$

for the EI case and

$$\mathcal{S}^2 \begin{cases} v_1 = A_1 s_\gamma \cos(\delta p_2 X_1) + B_1 c_\gamma \sin(\delta p_2 X_1) \\ v_2 = A_2 c_\gamma \cos(\delta p_2 X_1) + B_2 s_\gamma \sin(\delta p_2 X_1) \end{cases} \quad \text{or} \quad \mathcal{A}^2 \begin{cases} v_1 = C_1 c_\gamma \cos(\delta p_2 X_1) + D_1 s_\gamma \sin(\delta p_2 X_1) \\ v_2 = C_2 s_\gamma \cos(\delta p_2 X_1) + D_2 c_\gamma \sin(\delta p_2 X_1) \end{cases} \quad (\text{D8})$$

for the EC case. Here, $(A, B, C, D)_j$ are real constants and $s_{\{b\}} = \sinh(\{b\} p_2 X_1)$ and $c_{\{b\}} = \cosh(\{b\} p_2 X_1)$. Incremental equilibrium (D1) together with the incremental boundary conditions (60) provide solutions in form of the critical stretch $\lambda_2 = \lambda_c^{(j)}$ and corresponding buckling mode $\Delta \mathbf{u} = \Delta \mathbf{u}^{(j)}$. For further technical details we refer to Reference 69. For the two bifurcation problems considered in this work the numerical values for the critical stretches are provided in Table D1.